Investigating REV-ERBβ Binding Pocket Dynamics with Implications for Rational Design of Small Molecule Modulators

Shriyansh Srivastava[1], Rakesh Thakur[1], Vishnu A.M.[1], Ashutosh Srivastava[1]*

[1]Department of Biological Sciences and Engineering, Indian Institute of Technology Gandhinagar-382355, Gujarat, India

*e-mail: ashutosh.s@iitgn.ac.in

Abstract

REV-ERBβ is a nuclear receptor (NR) with heme as an endogenous ligand that regulates its transcriptional activity. With key role in cellular functions such as glucose metabolism, immune response and dysregulation in pathologies such as Type-2 diabetes mellitus and obesity, small molecules targeting REV-ERBs have been discovered with agonist and antagonistic effect. However, due to lack of crystal structures in complex with these compounds, the structural and dynamical basis of these activities still remains elusive and hinders rational design of molecules targeting REV-ERB. Using molecular dynamics simulations and docking studies, we have characterized the dynamics of REV-ERBβ ligand-binding domain (LBD) in different conformational states. The heme binding pocket within LBD remained closed in absence of a ligand and heme was found to stabilize its dynamics as well as nuclear co-repressor (NCoR) peptide binding. We further show that the binding of antagonist destabilizes the NCoR peptide binding to LBD mediated by loss of interactions with residues at the NCoR-REV-ERBβ interface. These findings could be utilized to design molecular scaffolds with better activity and selectivity against REV-ERBβ.

Keywords: **REV-ERBβ, NR1D2, Nuclear Receptors, Molecular Dynamics Simulation, Protein Contact Network, Circadian Rhythms**

1. Introduction

Nuclear receptors (NRs) belong to a class of receptors that mediate their action via modulation of transcription of the target genes. REV-ERBα and REV-ERBβ belonging to the nuclear receptor subfamily 1, group D (referred to as NR1D1 and NR1D2) act as transcriptional regulators by binding to the same DNA response element (consensus sequence-AGGTCA) as the Retinoic Acid Receptor (RAR) - Related Orphan Receptors (ROR)[1,2]. REV-ERBα and REV- ERBβ have been reported to regulate the expression of genes involved in crucial cellular functions such as circadian rhythms, metabolism, and immune system[3]. The role of REV-ERBs is central to regulate the expression of other core-clock proteins such as Brain and Muscle ARNT-Like 1 (BMAL1), which is activated by the ROR transcription factor. REV-ERBβ competes with ROR to bind the related orphan receptors element (RORE) binding sites of DNA to inhibit the transcription of BMAL1 (Fig. 1A)[4,5].

REV-ERBα and REV-ERBβ follow the domain architecture of NR superfamily of proteins with N-terminal DNA binding domain, followed by a linker and a C-terminal ligand binding domain. The ligand binding domain (LBD) possesses the binding pocket for ligands known to bind REV-ERBα/β (Fig. 1B). The binding pocket comprises residues in the N-terminal loop, Helix-3, Helix-5, β-sheet, Helix-7, and Helix-11 (Fig. 1C)[2]. Compared to other members of NR superfamily, REV-ERBs lack Helix-12 in the C-terminal region. Helix-12 is critical for the recruitment of coactivator peptides to promote transcription of target genes[1]. Thus, REV-ERBs can only function as transcriptional repressors of their target genes. Heme binds to REV-ERBα/β as the endogenous ligand, recruits the nuclear corepressor protein (NCoR) and together, the complex represses the transcription of downstream genes. NCoR recruitment is governed by two interacting domain motifs (ID1 and ID2) present in the NCoR receptor interaction domain (RID) and the complex further recruits histone deacetylases (HDAC-3), resulting in transcriptional repression[2,6,7].

The role of REV-ERB has been investigated in diverse cellular functions and its dysregulation has been reported in several pathologies, making it an attractive drug target. Efforts have been made to experimentally discover small molecules modulating the REV-ERB activity[8]. The small molecules discovered have been pharmacologically used to regulate the REV-ERB activity in several disease models such as Alzheimer's, Duchenne Muscular Dystrophy (DMD), type-2 diabetes mellitus (T2DM), obesity, HIV replication cycle, non-alcoholic fatty liver disease (NAFLD), and cancer[9–17]. While most studies have

reported the role of small molecules on α isoform, only a few studies have looked at the β isoform[8,18,19]. The ligands have primarily been discovered using fluorescence resonance energy transfer (FRET) and cellular gene reporter assays[20,21]. Though the effect of these compounds has been studied *in vitro* and *in vivo*, their binding modes and molecular basis have not been established due to the lack of experimentally derived complex structures.

Recently, the first structure of REV-ERBα in complex with a synthetic ligand STL1267 has been determined (PDB ID: 8D8I)[22]. The structure indicates the binding site of the ligand to be same as heme. However, it was observed that binding mode of synthetic ligand was different than heme. The synthetic ligand was more localized to the hydrophobic regions of the pocket. The NCoR ID1 formed antiparallel β-sheet interactions with Helix-11 residues, which is different than the binding mode in heme bound state (PDB ID: 6WMQ)[7]. Apart from this, no complex structures with synthetic ligands have been resolved for REV-ERBα or REV-ERBβ. In this study, we have analyzed the differences in the crystal structures of REV-ERBβ LBD in presence or absence of a ligand, following which, we used molecular dynamics (MD) simulations to understand the dynamics REV-ERBβ LBD in different states. Lastly, we have performed molecular docking and MD studies on small molecule complexes to understand their effect on NCoR binding.

2. Results

2.1 Crystal Structures of REV-ERBβ LBD Highlight Conformational Variability of Binding Pocket

Crystal structures of REV-ERBβ LBD have been resolved in three different states: Apo, heme-bound, and heme+NCoR bound (Fig. 1D and Supplementary Table S1). The endogenous ligand, heme, binds to the LBD of REV-ERBβ by forming coordination bonds with its iron center (Fe^{+3}) and residues C384 and H568 on either side of the binding pocket, at the N-terminal loop and Helix-11, respectively. In addition, the binding of heme is stabilized by other interactions at the N-terminal loop (H381, L382, V383, P385, M386), Helix-3 (W402, F405, F409, V413), Helix-5 (F443, L446, M447, F450), β-sheet (F454), loop before Helix-7 (G478, A479), Helix-7 (G480, L482, M486), Helix-11 (E571, L572), and C-terminal loop (F575) (Fig. 1C and Supplementary Table S2A)[23].

The NCoR binds to a REV-ERBβ dimer through ID1 and ID2 with each monomeric REV-ERBβ LBD subunit, respectively[7]. The residue, K421, located on Helix-3, is critical for NCoR recruitment and

interaction stabilization, supported by interactions of non-bonded contacts between REV-ERBβ LBD and ID1/2 peptides predominantly with Helix-3 and Helix-5 (Supplementary Fig. S1A-D and Supplementary Table S2B-C)[24].

To quantify the conformational differences between the crystal structures of REV-ERBβ LBD, we superimposed the individual chains of all the crystal structures and clustered them based on RMSD. The twelve chains corresponding to six PDB crystal structures formed two distinct clusters for Apo and bound form (Fig. 2). The bound cluster further formed distinct sub-clusters based on heme or heme+NCoR bound state (Fig. 2A-B). Considerable differences in Helix-3 and 11 were seen, wherein, helices in Apo form were bent inwards to occupy the vacant heme binding pocket. The position of binding site residues W402, F405, and F409 in Helix 3 were distant by 11.5Å, 8.5Å, and 3Å in heme bound form (3CQV) from their position in the Apo form (2V0V-A) (Fig. 2C). Furthermore, the distance between Cα atoms of W402-M447 (hereafter referred to as H3-H5 distance) for 2V0V-A and 3CQV were 15.3Å and 20.2Å, respectively. The distance between Cα atoms of W402-H568 (hereafter referred to as H3-H11 distance) for 2V0V-A and 3CQV were 13.2Å and 16.6Å (Fig. 2D). These observations combined with the clustering suggested that the binding pocket of REV-ERBβ LBD could take up different conformations based on the binding state.

2.2 Molecular Dynamics Simulations Reveal Conformational Flexibility of Ligand Binding Pocket

To understand dynamics of the binding site in Apo state, we performed three independent 1μs MD simulations of 2V0V-A. The RMSD of Cα atoms for the replicates remained stable around 3.5Å to 4.0Å, with some deviations in the beginning of the simulation (Supplementary Fig. S2A and Supplementary movie 1). Similarly, the radius of gyration for the simulation trajectories were found to be stable between 16.87Å to 17.25Å (Supplementary Fig. S2B). To further investigate the flexibility in different regions of protein, we calculated RMSF for the protein trajectory. Considerable fluctuations were observed for the residues in Helix-3, β-sheets, Helix-11, and C-terminal region including the heme binding site residues in Helix-3 (W402, F405, F409, V413) and Helix-11 (H568, E571, L572) (Fig. 3A).

The H3-H5 and H3-H11 distances (as described above) for the entire 2V0V-A trajectory showed some variation around the crystal structure distances suggesting that the binding pocket remains closed throughout the simulation (Fig. 3B). Notably, across all the simulations we did not observe any binding pocket

conformation similar to the heme bound state (Supplementary Fig. S2C-D). This could be due to the high energy barrier between the conformational states or an induced fit mechanism of heme binding to LBD. To further explore this, we performed MD simulations of the heme bound crystal structure after removing heme (hereafter referred to as Apo-3CQV). The Apo-3CQV additionally had N-terminal loop residues (residues: 381-395) in the structure that were unresolved in the 2V0V-A structure. The RMSD of Apo-3CQV Cα atoms ranged between 2.5Å to 5.0Å, with higher deviations in two replicates, suggesting conformational change during simulations (Supplementary Fig. S2E and Supplementary movie 2). Interestingly, the radius of gyration for all the replicates decreased by approximately 1Å, indicating the change in conformation to a more compact state (Supplementary Fig. S2F). Similar to 2V0V-A trajectory, the binding pocket conformations in Apo-3CQV trajectory were different than the conformation in heme bound state (Supplementary Fig. S2G-H). RMSF calculations revealed a higher flexibility in the loop regions for Apo-3CQV, when compared to 2V0V-A trajectory. In addition, slightly higher flexibility was observed for the N-terminal region of Helix-3 (residues: 396-409), Helix-4, Helix-5 (residues: 430-442), and β-sheet region (residues: 454-455) that includes the binding site region (Fig. 3A). These combined results suggested that REV-ERBβ LBD exhibits a high conformational diversity and may use induced fit mechanism for heme binding.

To understand the overlap of dynamics between the two Apo states, we performed principal component analysis and projected the trajectories on the first two principal components (PCs). The first three PCs (hereafter referred to as PC1, PC2, and PC3) together explained ~58% and ~67% of the variability in 2V0V-A and Apo-3CQV trajectories, respectively (Supplementary Fig. S2I-J and Supplementary Table S3). A higher PC1 value for Apo-3CQV highlighted a larger variance than 2V0V-A trajectory (Fig. 3C). The projections of 2V0A-A and Apo-3CQV trajectories on 2V0V-A eigenvectors suggested an overlap in the sampled conformational (Fig. 3D). We performed covariance overlap analysis for both the trajectories and confirmed this observation with a normalized overlap value of 0.34 along PC1 and PC2. The dominant motions comprised fluctuations in loop regions, Helix-3, β-sheets, Helix-11, and C-terminal region for both the trajectories. Primarily, Helix-3 and Helix-11 move to accommodate the vacant pocket in case of Apo-3CQV trajectories. This can also be observed in the H3-H5 and H3-H11 distances where Apo trajectory shows fluctuations around the crystal structure (9.2-18.4 Å and 7.6-18.5Å, for H3-H5 and H3-H11

respectively), but the Apo-3CQV trajectory shows considerable movement away from the crystal structure (13.5-23.6Å and 8.0-18.9Å respectively) (Fig. 3B). Overall, the global motions across three principal components were observed for regions near the binding pocket, including the key binding site residues at Helix-3 (W402, F405, F409, V413) and Helix-11 (H568, E571, L572) (Fig. 3E-F).

2.3 Heme Binding Stabilizes Binding Pocket Dynamics

REV-ERBβ LBD MD simulations in Apo and Apo-3CQV form revealed the dynamics of ligand binding pocket. In absence of the endogenous ligand, the conformationally open pocket transitioned into a closed Apo state, highlighting the heme-induced conformational changes. To further understand this phenomenon, we performed MD simulation for 3CQV crystal structure (with heme bound).

The heme iron center remained coordinated throughout the trajectory with C384 and H568 and the side chain interactions were stabilized by binding site residues (Fig. S3A-C and Supplementary movie 3). The solvent exposed propionate groups were flexible, but the overall heme structure remained bound in the pocket. From visual inspection, it was evident that flexible regions of the binding pocket at Helix-3 and Helix-11 remained relatively stable than Apo and Apo-3CQV counterparts (Supplementary Movie 3). The H3-H5 and H3-H11 distances also showed lower variation in these distances, complementing the visual observation (Fig. 3G-H). We also found lower residue-wise fluctuations in flexible regions of Helix-3, Helix-4, 5 and β-sheets in comparison to Apo and Apo-3CQV trajectories (Supplementary Fig. S3D). In addition, RMSD calculations showed that LBD structure was conformationally more stable than the Apo form (Supplementary Fig. S3E). These results suggested that heme binding stabilizes the dynamics of binding pocket at Helix-3 and Helix-11 and governs an overall conformational stability of REV-ERBβ LBD.

2.4 Heme confers stability to NCoR peptide interactions with LBD

Nuclear receptors are ligand-dependent transcriptional regulators where ligand binding causes recruitment of co-activator/repressor peptides. Mosure and colleagues reported that the binding of NCoR in presence of heme was governed by interactions of ID1/ID2 peptide with LBD (Fig. S1A-D and Supplementary Table S2B-C)[7]. The conserved I/LxxI/LI/LxxxI/L/F co-repressor NR motif (hereafter referred to as CoRNR) interacts with the AF2 surface formed by Helix 3 to 5[7] (ID1 motif: ITLADHICQIITQDF and ID2 motif:

GLEDIIRKALM). Previous studies have also reported that residues in Helix-3, 4, 5, and 11 (W402, F409, V413, K414, V417, K421, R427, V435, K439, L572, F575, K576) regulate NCoR binding[25–27].

Based on our simulation results and these observations, we hypothesized that heme binding would induce a conformational state that stabilizes NCoR interactions *via* ID1/ID2 peptide with the AF2 surface. To test this, we performed MD simulations of REV-ERBβ LBD in complex with heme and NCoR ID1 and ID2 peptide (PDB ID: 6WMQ and 6WMS, respectively).

Similar to the 3CQV trajectory, heme remained coordinated and bound in the pocket for 6WMQ-A and 6WMS-A trajectories (Fig. S4A-B and Supplementary movies 4-5). The heme side chains were flexible and hydrophilic propionate group showed differential interactions. The propionate group in 6WMQ-A trajectory interacted with E571, while it rotated towards the N-terminal loop region forming contacts with H381 and C384 in 6WMS-A trajectory (Supplementary Fig. S4C-D). We further looked at the dynamics of ID1 and ID2 peptides. The ID peptides remained bound at the AF2 surface formed by residues at Helix-3, Helix-4, and Helix-5. The ID1 peptide contacts with key residues (V413, K414, V417, K421, L438, K439) were present throughout 6WMQ-A trajectory, suggesting the conservation of LBD-CoRNR motif interactions. The imidazole ring of histidine (H2261) in ID1 remained in contact with W402 (Helix-3) for a larger part of the simulation. The N-terminus of ID1 peptide additionally interacted with residues in the C-terminal region of LBD including residues in Helix-10 and Helix-11 (R565, N566, S569, L572, K576) for the initial part of simulation (Fig. 4A). The ID2 peptide from 6WMS-A trajectory exhibited interactions with Helix-3 (W402, F409, V413, K414, V417) and Helix-4 (H432, V435, L438, K439), including the AF2 surface residues (Fig. 4B).

To further characterize the role of heme in NCoR binding, we performed MD simulations for chain A of 6WMQ and 6WMS after removing heme (hereafter referred to as Apo-6WMQ-A and Apo-6WMS-A) (Supplementary movies 6-7). We observed key differences in LBD-ID peptide interactions upon comparative analysis of the trajectories (6WMQ-A v/s Apo-6WMQ-A and 6WMS-A v/s Apo-6WMS-A). In the absence of heme (Apo-6WMQ-A), we found loss of ID1 peptide interactions with key AF2 surface residues (K421, F426) and slight decrease in interactions with residues at Helix-3 and Helix-4 (K414, V417, L438) than in heme-bound trajectory (6WMQ-A). Further, the interactions of ID1 peptide N-terminus with Helix-10, Helix-11 and C-terminal were prominent throughout the Apo-6WMQ-A trajectory but were lost in

the later part of heme-bound trajectory (6WMQ-A) (Fig. 4C and 4A). Previous studies have reported differences in the binding mode of ID1 N-terminus, where it formed antiparallel β-sheets in Apo REV-ERBα isoform LBD crystal structure (PDB ID: 3N00)[28]. This sheet formation was lost in structures of REV-ERBβ LBD co-bound with heme and ID1 peptide, highlighting difference in ID1 N-terminus interactions upon ligand binding[7]. The interactions of ID2 peptide remained similar at AF2 surface in both trajectories (Apo-6WMS-A and 6WMS-A) (Fig. 4D and 4B). However, a slight increase in interactions with residues V417, K421 and decrease with residues F409, K414 were observed in absence of heme. The LBD-peptide contact analysis highlighted changes in ID peptide interactions with LBD in different states. Interestingly, we observed a higher RMSF for Cα atoms of ID1 peptide residues interacting at the AF2 surface (ITQDF) in Apo-6WMQ-A trajectory compared to its heme-bound counterpart (6WMQ-A) (Fig. 4E). These residues represented a part of CoRNR motif, highlighting increased fluctuations in absence of heme. Similarly, RMSF calculations for ID2 peptide Cα atoms in Apo-6WMS-A and heme-bound counterpart (6WMS-A) trajectories revealed higher fluctuations when heme was removed (Fig. 4F). Overall, the dynamics of ID peptides in presence or absence of heme proved the role of heme in stabilizing the LBD-NCoR complex interactions at the AF2 surface and revealed the dynamic behavior of ID1 N-terminus.

2.5 Molecular Docking and Simulation Reveals Differential Binding Mode of Agonists and Antagonists with REV-ERBβ LBD

Both REV-ERB α and β have emerged as potential drug targets in diverse diseases[3]. Interestingly, both agonists and antagonists have been discovered for REV-ERB[8]. As per the current understanding both agonists and antagonists bind REV-ERB LBD at the same (heme) binding pocket. However, the molecular basis of differential mechanisms of the two class of ligands has not been understood. Based on the above results we can hypothesize that the agonists, mimicking the action of heme, would positively affect the NCoR recruitment whereas antagonists would make the NCoR binding weaker. To investigate the conformational variations induced by the synthetic ligands (agonists and antagonists) in context of their function, we performed molecular docking and simulations. Since no crystal structure for REV-ERBβ LBD co-crystalized with a synthetic ligand has been resolved, we used Apo-3CQV structure for initial molecular

docking studies. The recently released crystal structure of REV-ERBα LBD co-crystallized with a synthetic ligand STL1267 (agonist) was used to validate our docking protocol (Supplementary Fig. S5A)[22]. We performed docking studies using experimentally discovered small molecule agonists and antagonists against REV-ERB reported in ChEMBL database (Supplementary file 1). We found that docking score (hereafter referred to as Dscore) ranged from –10.57 to 0.103 for agonists and –9.763 to –2.292 for antagonists (Supplementary file 1). The top 3 agonists, CHEMBL2030069, CHEMBL2059573, and CHEMBL2030068 had comparable docking scores (Table 1). However, the H-bond, Pi-Pi stacking, and salt bridge interactions were different, but non-bonded hydrophobic interactions remained similar (Fig. 5A). To assess the dynamics of protein-ligand complexes, we performed simulations for each complex. The ligands were flexible during the trajectory run but remained within the pocket (Supplementary Fig. S5B, and Supplementary movies 8-10). The protein-ligand contact timeline analysis showed that although the binding site is similar, the molecules were stabilized by different interactions. CHEMBL2030069 and CHEMBL2030068 interacted with the binding site residues in Helix-3, Helix-5, and Helix-11 (W402, F405, F409, F443, H568, L572) while CHEMBL2050573 interacted with residues in the N-terminal loop, Helix-7, and Helix-11 (H381, V383, C384, P385, M386, L482, H568, E571) (Fig. S5D-F). A similar differential interaction trend was seen for the top 3 antagonists: CHEMBL3590561, CHEMBL3590571, and CHEMBL3590573; where CHEMBL3590561 interacted with residues in N-terminal loop, Helix-3, 11, and C-terminal region (C384, F405, F409, H568, E571, F575). Antagonists CHEMBL3590571 and CHEMBL3590573 interacted with residues F405, F443, F575 and W402, F575, respectively (Fig. 5B, Supplementary Fig. S5C, S5G-I, Supplementary Table 1, and Supplementary movies 11-13). Although there were variations in the binding modes of different molecules, we could not observe any specific difference between the interactions of agonists and antagonists in the Apo-3CQV pocket. This was expected as the binding pocket for both class of molecules is same, and the differential functional effect is perhaps a consequence of the differential dynamics in complex with NCoR.

2.6 Differential Binding Modes of Top Ranked Agonists and Antagonists with Apo-6WMQ-A and Apo-6WMS-A

To understand if the binding of agonists and antagonists differentially affects the NCoR binding, we docked

the top three agonists and antagonists identified in previous section to Apo-6WMQ-A and Apo-6WMS-A. Interestingly, in case of Apo-6WMQ-A, the docking score and interactions of two out top three agonists (CHEMBL2030069 and CHEMBL2030068) were different from Apo-3CQV while one agonist (CHEMBL2059573) docked in the core of binding pocket with interactions similar to Apo-3CQV docked complex (Supplementary Fig S6A). In case of Apo-6WMS-A, the docking scores, and interactions for the three agonists were similar to Apo-3CQV (Supplementary Fig S6B). The docking score and interactions for the top three antagonists (CHEMBL3590561, CHEMBL3590571, CHEMBL3590573) had a similar trend as that of Apo-3CQV docked complex. The molecules docked within the core of binding pocket for both Apo-6WMQ-A and Apo-6WMS-A structures (Supplementary Fig. S6C-D). The docking score for the top 3 agonist and antagonist molecules are summarized in Table 1.

To further focus on the effect of agonist and antagonist binding on the LBD-ID interactions, we analyzed the interactions of CHEMBL2059573 (hereafter referred to as agonist) and CHEMBL3590561 (hereafter referred to as antagonist) with REV-ERBβ LBD in detail. The agonist and antagonist were structurally different belonging to the class of tertiary amine and diarylalkylamine derivative, respectively (Fig. 6A-B)[19,29]. In Apo-6WMQ-A agonist docked complex; the p-chlorobenzene ring oriented to the solvent exposed region. Several hydrophobic interactions were seen between nitrothiophene ring and N-terminal loop, loop before Helix-7, and Helix-7 residues (H381, L382, V383, C384, P385, M386, A479, L482, L483, M486). The bulky phenyl urea-carbamate moiety was stabilized primarily by the binding site residues at Helix-3, Helix-5 and Helix-11 (W042, F405, F409, V413, T442, F443, L446, M447, L572, F575) while the central nitrogen atom of tertiary amine group formed H-bond interactions and salt-bridge with Helix-11 residues (H568 and E571) (Fig. 6C). In contrast, antagonist docked to Apo-6WMQ-A oriented deeper into the binding pocket, distal to Helix-3. The fluorophenyl ring formed Pi-Pi stacking interaction with H568, and the cyclopentanamine-phenyl moiety formed H-bonds with E571. The hydrophobic interactions of methyl-piperazine group with N-terminal loop, Helix-5, β-sheets, Helix-7, and Helix-11 residues (H381, L382, V383, C384, P385, M386, T442, F443, L446, M447, F450, L453, F454, A479, L482, L483, M486, L572, F575) further stabilized the docked molecule (Fig. 6D).

The binding mode of agonist to Apo-6WMS-A was similar to Apo-6WMQ-A docked complex (Fig. 6E). However, the antagonist exhibited differences in binding. In Apo-6WMS-A antagonist docked complex,

CHEMBL3590561 orientation was more compact and mimicked heme-like conformation. The fluorophenyl and methyl piperazine were deeper in the pocket, surrounded by the hydrophobic cluster residues, while cyclopentanamine-phenyl moiety remained towards the outer side of the binding pocket. Pi-Pi stacking was observed between fluorophenyl ring and F443 at Helix-5. Salt-bridges were formed between nitrogen adjacent to cyclopentane ring and C384, and hydrogen bonds with C384, H568. Another salt bridge was formed between nitrogen of methyl piperazine and C384 (Fig. 6F). A summary of the interactions can be found in Supplementary file 1. Overall, several crucial differences were observed in binding of agonist and antagonist to the NCoR bound REV-ERBβ LBD.

2.7 MD Simulations Reveal Impact of Agonist and Antagonist on Pocket Dynamics and ID Peptide Interactions with REV-ERBβ LBD

From previous MD simulation results (6WMQ-A, 6WMS-A, Apo-6WMQ-A, Apo-6WMS-A) we could comprehend changes in the interactions of ID1/2 peptide at AF2 surface in presence or absence of heme. We hypothesized that binding of agonist or antagonist could also modulate these interactions, forming the structural basis of their pharmacological activity. To check our hypothesis, we performed MD simulations for Apo-6WMQ-A and Apo-6WMS-A complexed with agonist (CHEMBL2059573) or antagonist (CHEMBL3590561) (here after referred as Apo-6WMQ-A-agonist, Apo-6WMQ-A-antagonist, Apo-6WMS-A-agonist, and Apo-6WMS-A-antagonist).

In all the simulations, the small molecules remained within the binding pocket but were flexible (Supplementary Fig. S7). In Apo-6WMQ-A-agonist trajectory, agonist was central to the binding pocket, with dominant interactions in N-terminal loop (L382, M386), Helix-3 (W402, F405, F409), Helix-5 (F443, L446), and Helix-7 (G480, M486), Helix-11, C-terminal region (H568, E571, F575) and ID1 peptide (H2261). In contrast, antagonist predominantly interacted with residues in Helix-5 (F443, F450), Helix-7 (A479, L482) and Helix-11 (H568, E571) and lost interactions with residues in Helix-3 in later part of the Apo-6WMQ-A-antagonist trajectory (Supplementary Fig. S7A-B and Supplementary movie 14-15).

In case of Apo-6WMS-A-agonist/antagonist trajectories, agonist interacted with residues in N-terminal loop (L382, C384, M386), Helix-3 (W402, F405, F409), Helix-5 (F443, L446, F450), Helix-7 (G480, M486), Helix-11 (H568, L572), C-terminal region (F575) and ID2 peptide (L2262); while antagonist mimicked

heme-like conformation and interacted predominantly with residues in N-terminal loop (C384), Helix-3 (F405, F409), and Helix-11 (H568 and F575) (Supplementary Fig. S7C-D and Supplementary movie 16-17). From visual inspection of trajectories (Apo-6WMQ-A-agonist, Apo-6WMQ-A-antagonist, Apo-6WMS-A-agonist, and Apo-6WMS-A-antagonist), we could identify a higher degree of motion in N-terminal loop, Helix-3, Helix-11, and C-terminal regions compared to rest of the LBD structure (Supplementary movie 14-17). We calculated RMSF of LBD Cα atoms to understand residue-wise fluctuations for the four systems (Apo-6WMQ-A-agonist, Apo-6WMQ-A-antagonist, Apo-6WMS-A-agonist, and Apo-6WMS-A-antagonist) and compared them with their respective Apo and heme-bound trajectories.

We observed higher fluctuations for Cα atoms of LBD in N-terminal loop, initial Helix-3 (residues: 391-413), Helix-5, β-sheet (residues: 446-463), loop before Helix-6, Helix-6 (residues: 467-480), Helix-11, and C-terminal region (residues: 568-577) in Apo-6WMQ-A-antagonist trajectory as compared to other systems (Apo-6WMQ-A, 6WMQ-A, Apo-6WMQ-A-agonist) (Fig. 7A). However, in the case of 6WMS trajectories (Apo-6WMS-A, 6WMS-A, Apo-6WMS-A-agonist, Apo-6WMS-A-antagonist), we did not see such differences. A higher fluctuation in Helix-11 and C-terminal regions (residues: 568-577) was observed in Apo-6WMS-A-agonist and Apo-6WMS-A-antagonist trajectories compared to other systems. In addition, Apo-6WMS-A-agonist exhibited minor fluctuations in distal Helix-3 (residues: 405-423) (Fig. 7B).

We further calculated RMSF of Cα atoms of ID1/2 peptide for all models and compared them with respective Apo and heme bound forms. Importantly, we observed a higher RMSF for ID1 N-terminus (residues: 1-6) (~2-6 Å) in antagonist bound state, as compared to the counterparts (Fig. 7C). Similarly, RMSF calculations identified a higher fluctuation of ID2 peptide in Apo-6WMS-A-antagonist (Fig. 7D).

From protein-ligand contact map and contact timeline analysis for ID peptides, we could observe loss in interactions of ID1 peptide with residues located in Helix-10, Helix-11, and C-terminal region (residues: N565, N566, S569, K576) after ~50 ns in Apo-6WMQ-A-antagonist compared to Apo-6WMQ-A-agonist trajectory (Fig. 7E-F and Supplementary Fig. S7E-F). We did not find such differences upon comparative analysis of Apo-6WMS-A-agonist/antagonist trajectories (Fig. 7G-H and Supplementary Fig. S7G-H).

Further, it was visible from Apo-6WMQ-A-antagonist trajectory that Helix-11 moved farther as compared to the initial structure (Supplementary movie 15). This visual observation was confirmed by calculating the H3-H11 distance for Apo-6WMQ-A-antagonist trajectory. After ~50 ns, the distance increased to ~21 Å and

remained in that range. However, such large deviations were not observed in distances for Apo-6WMQ-A-agonist, Apo-6WMS-A-agonist, or Apo-6WMS-A-antagonist trajectories (Supplementary Fig. S7I). Our initial observations suggested small molecule binding affect REV-ERBβ LBD and ID peptide dynamics.

To quantify the effect of structural changes on binding of ID peptide, we calculated ID1/2 peptide binding affinity in respective simulation trajectories, with heme bound trajectory as positive control (see Methods). We observed a significant decrease in ID1/2 peptide binding affinity in presence of antagonist as compared to agonist bound counterparts. The ID1 peptide binding affinity in Apo-6WMQ-A-agonist trajectory ranged –9.622 to –8.763 kcal/mol while it decreased in Apo-6WMQ-A-antagonist trajectory (–8.398 to –7.532 kcal/mol). We observed a comparable ID1 binding affinity value in heme bound 6WMQ-A trajectory (–8.563 to –7.939 kcal/mol) (Fig. 7I). Similarly, ID2 peptide binding affinity in Apo-6WMS-A-agonist ranged –7.596 to –7.072 kcal/mol which decreased in Apo-6WMS-A-antagonist trajectory (–7.434 to –6.582 kcal/mol). The ID2 peptide binding affinity in heme bound 6WMS-A trajectory ranged –6.953 to –6.573 kcal/mol (Fig. 7J).

Overall, these combined results suggested that structural changes induced by agonist favored, while the changes upon antagonist binding reduced REV-ERBβ LBD-ID peptide binding affinity.

2.8 Network Analysis Reveals Differential ID Peptide Interactions in Agonist/Antagonist Bound Trajectories

From the analysis of simulation trajectories, it was revealed that binding of small molecules directly affected the binding of ID1/2 peptide to the REV-ERBβ LBD. However, the results did not capture the residue level interaction in comprehensive detail. To understand the effect of small molecule binding on interactions between ID peptide and REV-ERBβ LBD at residue-level, we constructed protein contact network (PCN) and inferred interactions between residue pairs. We quantified the edge frequency (represented as edge weights, see Methods) between ID1/2 peptide (chain E in complex) and REV-ERBβ LBD (chain A in complex) in the PCNs created for trajectory frames in agonist/antagonist bound states (Apo-6WMQ-A-agonist, Apo-6WMQ-A-antagonist, Apo-6WMS-A-agonist, and Apo-6WMS-A-antagonist) (Fig. 8A).

It was observed that the number and frequency of unique edges in antagonist frames were lower as compared to the agonist counterparts (Fig. 8B and Table S4). We found 15 and 14 unique edges between

ID1 peptide and REV-ERBβ LBD in Apo-6WMQ-A-agonist and Apo-6WMQ-A-antagonist frames, respectively. The ID1 N-terminus residues I2256, T2257, and L2258 exhibited high frequency edges with Helix-4, Helix-10 and Helix-11 residues (A440, N565, N566, S569, L572, 573) in Apo-6WMQ-A-agonist frames. In contrast, except for the edges between I2256-L572 and I2262-V413, the edge frequencies for Apo-6WMQ-A-antagonist frames was lower, highlighting weaker interactions (Table S4). We next compared the frequency of edges common to both the trajectory frames. Consistent with the findings for unique edges, we found a decrease in frequencies of the common edges for Apo-6WMQ-A-antagonist frames (Fig. 8C and Table S5A). Interestingly, the common edges involved residues from CoRNR motif (I2262-F2270) and AF2 surface (Helix-3 to 5) interactions, and a decrease in the edge frequency further proved the effect of antagonist binding on disrupting the interactions.

Similarly, the Apo-6WMS-A-agonist and Apo-6WMS-A-antagonist frames exhibited 8 and 4 unique edges between ID2 and REV-ERBβ LBD (Fig. 8C and Table S5B). The unique edges comprised interactions between CoRNR motif and AF2 residues and generally exhibited a lower frequency in both cases. The common edges between Apo-6WMS-A-agonist and Apo-6WMS-A-antagonist frames were also present at the AF2 interacting regions. However, the decrease in edge frequency for antagonist frames were not consistent as observed in ID1 counterpart (Apo-6WMQ-agonist/antagonist). For example, the edge frequencies for some pairs increased (I2262-K439, I2266-K439, L2270-V417), decreased (L2270-K414, R2267-V435), and remained unchanged (E2263-K439, I2265-T410, A2269-V417) (Fig. 8C and Table S5B). These initial results from protein contact network highlighted the direct impact of small molecule binding on ID peptide and REV-ERBβ LBD interactions.

To understand the role of changes in edge frequency on the local and global architecture of ID peptide and REV-ERBβ LBD, we performed community structure analysis on PCNs obtained above. Community structure analysis has been used widely to understand the protein architecture and its direct relevance on functionality[30–32].The communities in a protein contact network are represented by the group of highly connected nodes within a region than other regions of a protein. We performed community structure detection using Louvain algorithm[33] for the four networks and compared them for Apo-6WMQ-A-agonist/antagonist and Apo-6WMS-A-agonist/antagonist. All the four PCNs formed 10-12 communities.

In case of Apo-6WMQ-A-agonist, residues from the N-terminal loop of LBD, β-sheet regions, loop regions, and Helix-6 formed the largest community C1 (in orange) with 37 members, followed by the second largest community C10 (in grey) which includes residues from Helix-10, Helix-11, C-terminal loop, and three residues from the ID1 peptide (I2256, T2257, L2258) (Fig. 9A).

On the other hand, Apo-6WMQ-A-antagonist formed 10 communities as compared to 11 communities in Apo-6WMQ-A-agonist (Fig. 9A-B). Consistent with our previous results, all the residues in ID1 peptide formed a separate community C10 in Apo-6WMQ-A-antagonist, suggesting weaker/lesser interactions between the ID peptide and REV-ERBβ LBD (Fig. 9B and Table S6). In Apo-6WMQ-A-antagonist, we observed some major changes in the community membership. Residues in community C9 of Apo-6WMQ-A-agonist (marked with red dotted lines in Fig. 9A) reorganized to community C8 (marked with blue dotted line in Fig. 9B) in Apo-6WMQ-A-antagonist. Another major change in community membership was observed in communities C9 and C10 (marked with orange dotted lines in Fig. 9A) in Apo-6WMQ-A-agonist that formed a single community C9 in Apo-6WMQ-A-antagonist. The community membership of Apo-6WMQ-A-agonist/antagonist can be seen in Table S6.

In Apo-6WMS-A-agonist and antagonist, we observed 12 and 10 communities respectively. Unlike ID1 peptide in Apo-6WMQ-A-agonist, ID2 peptide did not form a community with the LBD in Apo-6WMS-A-agonist. (Supplementary Fig. S8 and Table S7). Similar to Apo-6WMQ-A-antagonist, ID2 peptide did not form a community with LBD in Apo-6WMS-A-antagonist. In the case of Apo-6WMS-A-antagonist, we also observed major changes in the community membership like Apo-6WMQ-A-antagonist. Residues present in communities C1 and C6 of Apo-6WMS-A-agonist (marked with red dotted line in Supplementary Fig. S8A) reorganized to form single community C1 (marked with blue dotted line in Supplementary Fig. S8B) in Apo-6WMS-A-antagonist. Other than this, there were some minor changes in the community membership (Table S7).

The merging and reorganization of the communities in antagonist bound trajectory suggested an increased communication within the LBD residues and loss of communication with ID peptide residues. Structurally, the community restructuring in Apo-6MWQ-A-agonist/antagonist trajectories can be attributed to differences in interactions of ID1 peptide with Helix-11 and C-terminal residues.

Overall, the change in local architecture of community harboring ID peptide, REV-ERBβ LBD nodes, and global reorganization within the REV-ERBβ LBD were indicative of residue level changes in the functional protein regions in presence of small molecules, further corroborating the previous results.

3. Discussion

Nuclear receptors have been an attractive target for drug discovery. As such, the role REV-ERB in several disease pathologies and maintenance of circadian rhythm have been well established. Leveraging the potential of REV-ERB as a drug target has led to the development of small molecules that can regulate its downstream transcriptional activity. While experimental studies have identified modulators of REV-ERB, the structural mechanisms of their pharmacological activity have remained elusive. Using computational methods to understand the structural mechanisms of small molecule activity, we have first reported the dynamic behavior of REV-ERBβ LBD in presence or absence of the endogenous ligand, heme. Following the initial observations, we have characterized the role of heme in regulating the global dynamics of LBD and the binding of NCoR ID1/2 peptides. The first key observation from the MD simulations of Apo-form (2V0V-A), holo-form after removing heme (Apo-3CQV), and heme-bound state (3CQV) highlighted the critical role of presence of a ligand. The pocket in Apo-3CQV closed during the simulation and adopted conformations similar to Apo-form, suggesting that presence of a ligand is essential for the LBD domain to remain in a functional state. Recent crystal structures and experiments have demonstrated the role of endogenous ligand heme to thermodynamically regulate binding of NCoR *via* ID1/2 peptide. The holo-conformation of the LBD was present throughout the 3CQV trajectory, suggesting that ligand binding may follow an induced fit model of binding. Higher fluctuations in 2V0V-A and Apo-3CQV trajectories compared to 3CQV trajectory further highlight the role of heme to stabilize the LBD, which is in line with the observed mechanism for other NR ligands[2]. In addition, MD simulations of ID peptide bound structures in presence and absence of heme further revealed the dynamic behavior of ID-LBD interactions, and the role of heme to stabilize key interactions for ID1 and ID2 peptides. Understanding these observations highlighted that utilizing the bound form conformation could be more useful for the structure based rational designing of small molecules to target REV-ERBβ. This hypothesis is further supported by our findings from molecular docking and MD simulations of small molecule ligand complexes.

Previously discovered small molecules modulating REV-ERB activity have been identified using FRET-based and cellular gene reporter assays that could indirectly highlight the regulation of REV-ERB activity with only a few computational studies on REV-ERBα[34,35]. Our study complements these experimental observations and establishes an understanding on the structural basis of the molecular effect exhibited by small molecule agonists and antagonists. Our initial findings from molecular docking and MD simulations revealed a difference in the binding modes for agonist and antagonist molecules within the orthosteric binding pocket.

The binding mode of top-ranked agonist (CHEMBL2059573) in our study was in line with a previous computational study investigating binding mode of agonist with REV-ERBα where interactions with Helix-3 phenylalanine residues were favorable for activity[34]. However, the binding mode of antagonist (CHEMBL3590561) in our study exhibited some differences from a recently published study predicting binding of prototypical synthetic antagonist SR8278 with REV-ERBα through GaMD simulations[35]. In our study, the binding mode of top-ranked antagonist was distal to Helix-3, however, GaMD studies revealed significant interactions with Helix-3, Helix-5 and Helix-6 residues in REV-ERBα. The difference in binding mode can be attributed to the difference in the chemical scaffold of antagonists under investigation. Through MD simulations of top-ranked agonist and antagonist from molecular docking screen, we were able to see a direct effect of differences in the binding mode of small molecules on ID1/2 binding dynamics with the LBD. The disruptions of ID1 N-terminus-LBD interactions, an overall higher RMSF for ID2 peptide in presence of antagonist, and differential dynamics induced by agonist and antagonist, evinced the plausible mechanism for the pharmacological activity. In addition, we were able to delineate the residue-level changes in presence of agonist/antagonist and capture local as well as global changes in the conformations using network analysis.

Given that we have biochemical screens for development of newer small molecules, this structural evidence for designing better molecules could be pivotal. This structural understanding is needed because studies have reported contrasting results for a small molecule, that has been identified an agonist in one study, but antagonist in another[36,37]. Similarly, the activity of SR9009, a prototypical agonist for REV-ERB has recently been reported to cause downstream effects in a REV-ERB independent manner[38]. In addition, with

the discovery of newer chemical scaffolds, understanding the structural basis of activity could be an effective tool for optimizing lead compound synthesis.

Lastly, the structural mechanisms identified from the current study can be critical to develop isoform selective REV-ERB modulators that has recently gained interest[39]. Even with binding site residues being conserved in the isoforms, the LBD only share ~71% similarity, which may give rise to functional conformational differences while recruiting NCoR *via* ID1/2. Further, a stark difference can be observed in LBD of isoforms, wherein the N-terminal loop harboring C384, critical for heme coordination is present in REV-ERBβ LBD but is unresolved in the α-isoform[7,22]. The conformation of N-terminal loop remains stable in the Apo-3CQV trajectory suggesting that it may have additional role in stabilizing the pocket. From the results of molecular docking and MD simulations of small molecules, we could observe that residues within the loop also interact with small molecules, supporting their functional relevance. Although this study is aimed at investigation of REV-ERBβ LBD, a qualitative comparison with REV-ERBα LBD co-crystallized with STL1267 (PDB ID: 8D8I) suggests that the conformation of N-terminal loop also has direct implications on NCoR binding. The unresolved conformation of N-terminal loop allows STL1267 to be buried deep into the binding pocket; because of which the ID1 peptide forms an antiparallel β-sheet similar to REV-ERBα Apo form (PDB ID: 3N00)[28]. Evaluating these hypotheses would aid in better understanding of the structural mechanisms underlying pharmacological activity. With the crystal structures resolved for both isoforms, a comparative structural study on experimentally discovered small molecules could strengthen the niche to develop isoform selective modulators.

4. Methods

4.1 Crystal Structure and Small Molecule Data Curation

The crystal structures for REV-ERBβ LBD (Uniprot accession number Q14995) were retrieved from protein data bank (PDB)[40,41]. The details of all the structures are summarized in Supplementary Table S1.

The dataset of small molecules experimentally evaluated against either isoform of REV-ERB protein was retrieved from the ChEMBL database[42]. The SMILES files for compounds associated with REV-ERBα (CHEMBL1961783) and REV-ERBβ (CHEMBL1961784) were downloaded. The compounds were sorted by their pharmacological property, based on the reported literature (Supplementary file 1).

4.2 Comparison of Crystal Structures

The crystal structures of REV-ERBβ LBD were split into individual chains resulting in twelve monomeric chains. These monomeric chains were superimposed and pairwise RMSD between the chains were calculated using UCSF-Chimera[43]. Hierarchical clustering was performed based on the RMSD matrix. Distances were computed between W402, F405, and F409 Cα atoms for 2V0V-A and 3CQV to quantify positional difference in crystal structures using PyMOL measurement wizard. Similarly, distances were also calculated for 2V0V-A and 3CQV crystal between Cα atoms of residues W402-M447 (H3-H5 distance) and W402-H568 (H3-H11 distance).

4.3 Identification of binding site residues

REV-ERBβ LBD heme bound crystal structure (PDB ID: 3CQV) was used to identify the binding site residues. The residues within the range of 5.0 Å of the heme present in the crystal structure were selected using zone selection tool in UCSF-Chimera[43] and identified as binding site residues (Supplementary Table S2A).

4.4 Molecular Dynamics Simulations

Molecular Dynamics (MD) simulations were performed for 2V0V-A and Apo-3CQV using GROMACS v2016.3 and v2021.3[44]. Pre-processing of the crystal structures was performed before setting up the system for MD simulations. Briefly, water molecules in the 2V0V-A were removed and the structure was further

minimized using UCSF Chimera with default parameters[43]. Apo-3CQV crystal structure was prepared using Protein Preparation Wizard (ProteinPrep) in Schrödinger with default parameters to replace selenomethionine residues with methionine, remove waters, add missing residue atoms, and minimize the structure (Schrödinger Release 2022-3: Protein Preparation Wizard; Epik, Schrödinger, LLC, New York, NY, 2022). The processed structures were used for MD simulations.

Same parameters for 2V0V-A and Apo-3CQV were used for simulations. In the simulations, each model structure was incorporated at the center of dodecahedron box with periodic boundary conditions and a minimum distance of 12Å between protein and the box boundary. TIP3P water model was used to solvate the system. The system was neutralized using Na^+ and Cl^- ions and further ions were added to maintain the ionic concentration of 0.15M. AMBER99SB-ILDN force field[45] was used during the simulations. Energy minimization was performed on the system for 1000 steps using Steepest Descent algorithm with maximum force cut-off set at 500 $kJmol^{-1}nm^{-1}$.

The energy minimized system was equilibrated before the final MD run. The equilibration was carried out in four steps. In the first step, NVT equilibration of 1ns was performed where v-rescale thermostat was used to maintain a constant temperature of 300K. In the second step, 1ns NPT run was performed using Berendsen barostat[46] to maintain the average pressure at 1 bar. In the third equilibration step, 1ns NPT was run using Parrinello-Rahman barostat[47] to maintain the pressure at 1 bar. Position restraints on all the heavy atoms were applied for these three equilibrations run. LINCS algorithm[48] was used for constraint on the bond length between atoms and Particle mesh Ewald method[49] was used to calculate long-range electrostatic interactions. In the last NPT run for 1ns, the system was equilibrated using Parrinello-Rahman barostat[50] without any position restraint on heavy atoms.

The equilibrated system was simulated for 1µs in triplicates (3 replicas). During MD production run, the temperature and pressure were maintained at 300K and 1 bar using v-rescale temperature and Parrinello-Rahman coupling method, respectively. The time-step for simulation was set to 2 fs with parameters such as energies, pressure, and temperature written after every 10 ps.

MD simulation of heme bound crystal structure (PDB ID: 3CQV) was performed using Desmond (Schrödinger Release 2022-3: Desmond Molecular Dynamics System, D. E. Shaw Research, New York, NY, 2022. Maestro-Desmond Interoperability Tools, Schrödinger, New York, NY, 2022). System builder

tool was used to set up the initial system for simulations with OPLS4 force field[51]. The system was simulated in rhombic dodecahedron xy-hexagon box with TIP3P water model as explicit solvent. The system was neutralized with Na^+ and Cl^- ions, and further ions were added to make the ionic concentration of 0.15 M. Molecular Dynamics tool in the Desmond module was used to minimize the energy and equilibrate the system with default parameters. The final MD run of 500ns was performed using NPT ensemble at 300K and 1.01325 bar pressure and selecting the option to relax the model system before simulation (Desmond simulation settings). Similarly, 500ns MD simulations of heme+ID peptide bound crystal structures (PDB ID: 6WMQ and 6WMS) and 1μs MD simulations of Apo-6WMQ-A and Apo-6WMS-A were performed with Desmond simulation settings.

4.5 Analysis of protein trajectories

The replicates of 2V0V-A and Apo-3CQV trajectories were corrected for periodic boundary conditions, and then fitted on the first frame of their respective protein trajectory to negate the rotational and translational motions. Protein trajectory analysis was performed using in-built gmx functions. Root Mean Square Deviation (RMSD) calculations were performed for the Cα atoms of protein structure models using gmx rms. The first frame of respective trajectory was taken as the reference structure and RMSD was computed for all the replicates of both the trajectories. Residue-wise fluctuations were calculated as root mean square fluctuation (RMSF) for both protein trajectories using gmx rmsf. Radius of gyration (Rg) was calculated for all the replicates of trajectories to measure the protein compaction during simulation runs.

The three replicates of respective trajectories were concatenated; both 2V0V-A and Apo-3CQV trajectories comprised 30000 frames each. The trajectories were subsequently corrected for rotational and translational motions. Further analyses were performed on concatenated 2V0V-A and Apo-3CQV trajectories.

Principal component analysis (PCA) was performed using gmx covar and gmx anaeig. Briefly, gmx covar was utilized to construct a covariance matrix, calculate eigenvalues, and eigenvectors using the coordinates of the 2V0V-A backbone atoms. The protein trajectories were projected to their respective eigenvectors, and principal components were calculated with gmx anaeig function. The subspace overlap between 2V0V-A and Apo-3CQV eigenvectors were calculated using gmx anaeig. H3-H5 and H3-H11 distances for 2V0V-A and Apo-3CQV trajectories were calculated using gmx distance.

For 3CQV, 6WMQ-A and 6WMS-A trajectories, distances were calculated between the heme iron center (Fe^{+3}) with S-atom of C384 and N-atom of H568. H3-H5 and H3-H11 distances and further analyses were performed using measurement tool and Simulation Interactions Diagram (SID) analysis tool in Desmond module of Schrödinger, respectively (Schrödinger Release 2022-3: Desmond Molecular Dynamics System, D. E. Shaw Research, New York, NY, 2022. Maestro-Desmond Interoperability Tools, Schrödinger, New York, NY, 2022).

4.6 Molecular Docking

All molecular docking studies were performed in Schrödinger with OPLS4 force field (Schrödinger Release 2022-3: Maestro, Schrödinger, LLC, New York, NY, 2022)[51]. To establish the validity of our docking procedure, the crystal structure of REV-ERBα LBD (PDB: 8D8I) was used as control[22]. Briefly, the protein was prepared with the ProteinPrep protocol. The binding site residues were identified from crystal structure using the protocol mentioned above to generate the docking grid. The co-crystallized ligand was removed and further prepared by Ligand Preparation Wizard (LigPrep) module with default parameters for molecular docking (Schrödinger Release 2022-3: LigPrep, Schrödinger, LLC, New York, NY, 2022). Following this, STL1267 compound was re-docked in XP mode. RMSD of re-docked pose was calculated using co-crystallized ligand as a reference and interactions were compared.

Molecular docking was performed for agonist and antagonist molecules with the Apo-3CQV structure model. In the preprocessing step, the small molecules were prepared using the LigPrep module and the generated conformers were used for docking. The Apo-3CQV structure was prepared using the ProteinPrep protocol. The energy minimized protein structure was further processed by Receptor-Grid Generation tool to generate the docking grid with the centroid defined by the binding site residues. Standard precision (SP) docking was performed with the agonists and antagonists. Extra precision mode of docking (XP) was performed using top conformers of all the molecules using Ligand Docking tool in the Glide module of Schrödinger (Schrödinger Release 2022-3: Glide, Schrödinger, LLC, New York, NY, 2022). Based on the docking score in 3CQV docked complexes, the top three agonists and antagonists were selected and docked in XP mode to Apo-6WMQ-A and Apo-6WMS-A.

4.7 Molecular Dynamics Simulations of Top Score Docked Complexes

100ns MD simulations of docked complexes were carried out in Desmond module with Desmond simulation settings mentioned above (Schrödinger Release 2022-3: Desmond Molecular Dynamics System, D. E. Shaw Research, New York, NY, 2022. Maestro-Desmond Interoperability Tools, Schrödinger, New York, NY, 2022). Supplementary Table S8 gives the details of all the simulations performed in this study.

4.8 Analysis of Docked Complex Simulation Trajectories

Desmond simulation trajectories were analyzed using simulation interactions diagram (SID) analysis tool. Briefly, to evaluate the dynamics of small molecules, ligand ASL was set to 'small molecule (res.type UNK)' with protein set as 'protein (Chain.name A) and NCoR peptide (chain.name E)'. To analyze the dynamics of NCoR peptides, ligand ASL was set to 'chain.name E' with protein set as 'chain.name A' in the SID analysis tool selection. RMSF for Cα atoms of NCoR peptide (ID1/2) and LBD in different states was calculated to assess the residue-wise fluctuations across the simulation trajectories.

4.9 ID1/2 Peptide Binding Affinity Calculations from MD Simulation Trajectories

51 equally spaced frames were extracted from the last 100ns of heme bound (6WMQ-A and 6WMS-A) and last 40ns of agonist/antagonist bound trajectories (Apo-6WMQ-A-agonist, Apo-6WMQ-A-antagonist, Apo-6WMS-A-agonist, and Apo-6WMS-A-antagonist). Binding affinity for ID peptide (chain 'E' in complex) with REV-ERBβ LBD (chain 'A' in complex) in different states was calculated using PRODIGY (PROtein binDIng enerGY prediction) standalone package[52]. Briefly, chain A and chain E were selected for binding affinity calculations at 27°C. Non-parametric Mann-Whitney-Wilcoxon two-sided test was performed to compare the binding affinity values in different states using statannotations python package[53].

4.10 Protein Contact Network Construction and Network Analysis

Protein contact network (PCN) is a graph theoretic representation of 3D structure of a protein where nodes are usually defined by Cα atoms of amino acids and edges represent interatomic distance between Cα atoms based on a custom distance cutoff. The distance matrix is used to generate an adjacency matrix which takes

values 0 and 1 based on the distance between the Cα atom pairs. The Cα atom based PCN have been previously constructed at an interatomic distance of ≤7 Å which have successfully captured residue-level interactions to understand crucial information such protein structure-function relationships, impact of mutations, and allosteric communications[54].

We therefore constructed an undirected and weighted PCN with frames used in binding affinity analysis at a cutoff of ≤7 Å. The adjacency matrix for each frame was generated where $A_{ij} = 1$, if Cα atom pair lie within ≤7 Å distance, else $A_{ij}=0$ (if distance >7 Å and i=j, where i and j represent amino acid Cα atoms). The edge weights were calculated by summating the adjacency matrix for 51 frames followed by normalization. PDB files for each frame were parsed using Bio.PDB module from Biopython package[55]. PCN generation and downstream analysis were performed using in-built functions and algorithms as implemented in NetworkX[56].

5. References

1. Burris, T. P. *et al.* International Union of Basic and Clinical Pharmacology CXIII: Nuclear Receptor Superfamily-Update 2023. *Pharmacol Rev* **75**, 1233–1318 (2023).
2. Weikum, E. R., Liu, X. & Ortlund, E. A. The nuclear receptor superfamily: A structural perspective. *Protein Science* **27**, 1876–1892 (2018).
3. Kojetin, D. J. & Burris, T. P. REV-ERB and ROR nuclear receptors as drug targets. *Nat Rev Drug Discov* **13**, 197–216 (2014).
4. Ikeda, R. *et al.* REV-ERBα and REV-ERBβ function as key factors regulating Mammalian Circadian Output. *Sci Rep* **9**, 10171 (2019).
5. Guillaumond, F., Dardente, H., Giguère, V. & Cermakian, N. Differential Control of Bmal1 Circadian Transcription by REV-ERB and ROR Nuclear Receptors. *J Biol Rhythms* **20**, 391–403 (2005).
6. Raghuram, S. *et al.* Identification of heme as the ligand for the orphan nuclear receptors REV-ERBα and REV-ERBβ. *Nat Struct Mol Biol* **14**, 1207–1213 (2007).
7. Mosure, S. A. *et al.* Structural basis for heme-dependent NCoR binding to the transcriptional repressor REV-ERBβ. *Sci Adv* **7**, (2021).
8. Uriz-Huarte, A. *et al.* The transcriptional repressor REV-ERB as a novel target for disease. *Bioorg Med Chem Lett* **30**, 127395 (2020).
9. Roby, D. A. *et al.* Pharmacological activation of the nuclear receptor REV-ERB reverses cognitive deficits and reduces amyloid-β burden in a mouse model of Alzheimer's disease. *PLoS One* **14**, e0215004 (2019).
10. Welch, R. D., Billon, C., Valfort, A.-C., Burris, T. P. & Flaveny, C. A. Pharmacological inhibition of REV-ERB stimulates differentiation, inhibits turnover and reduces fibrosis in dystrophic muscle. *Sci Rep* **7**, 17142 (2017).
11. Yuan, X., Dong, D., Li, Z. & Wu, B. Rev-erbα activation down-regulates hepatic Pck1 enzyme to lower plasma glucose in mice. *Pharmacol Res* **141**, 310–318 (2019).
12. Solt, L. A. *et al.* Regulation of circadian behaviour and metabolism by synthetic REV-ERB agonists. *Nature* **485**, 62–68 (2012).
13. Borrmann, H. *et al.* Pharmacological activation of the circadian component REV-ERB inhibits HIV-1 replication. *Sci Rep* **10**, 13271 (2020).
14. Griffett, K., Hayes, M. E., Boeckman, M. P. & Burris, T. P. The role of REV-ERB in NASH. *Acta Pharmacol Sin* **43**, 1133–1140 (2022).
15. Griffett, K., Bedia-Diaz, G., Elgendy, B. & Burris, T. P. REV-ERB agonism improves liver pathology in a mouse model of NASH. *PLoS One* **15**, e0236000 (2020).
16. Wang, Y., Kojetin, D. & Burris, T. P. Anti-proliferative actions of a synthetic REV-ERBα/β agonist in breast cancer cells. *Biochem Pharmacol* **96**, 315–322 (2015).
17. Gomatou, G. *et al.* The Role of REV-ERB Receptors in Cancer Pathogenesis. *Int J Mol Sci* **24**, 8980 (2023).
18. Wang, S., Li, F., Lin, Y. & Wu, B. Targeting REV-ERBα for therapeutic purposes: promises and challenges. *Theranostics* **10**, 4168–4182 (2020).
19. De Mei, C. *et al.* Dual inhibition of REV-ERBβ and autophagy as a novel pharmacological approach to induce cytotoxicity in cancer cells. *Oncogene* **34**, 2597–2608 (2015).
20. Rasmussen, E. S., Takahashi, J. S. & Green, C. B. Time to target the circadian clock for drug discovery. *Trends Biochem Sci* **47**, 745–758 (2022).
21. Grant, D. *et al.* GSK4112, a Small Molecule Chemical Probe for the Cell Biology of the Nuclear Heme Receptor Rev-erbα. *ACS Chem Biol* **5**, 925–932 (2010).
22. Murray, M. H. *et al.* Structural basis of synthetic agonist activation of the nuclear receptor REV-ERB. *Nat Commun* **13**, 7131 (2022).
23. Pardee, K. I. *et al.* The Structural Basis of Gas-Responsive Transcription by the Human Nuclear Hormone Receptor REV-ERBβ. *PLoS Biol* **7**, e1000043 (2009).
24. Laskowski, R. A., Jabłońska, J., Pravda, L., Vařeková, R. S. & Thornton, J. M. PDBsum: Structural summaries of PDB entries. *Protein Sci* **27**, 129–134 (2018).

25. Burke, L. J., Downes, M., Laudet, V. & Muscat, G. E. O. Identification and Characterization of a Novel Corepressor Interaction Region in RVR and Rev-erbAα. *Molecular Endocrinology* **12**, 248–262 (1998).
26. Renaud, J.-P., Harris, J. M., Downes, M., Burke, L. J. & Muscat, G. E. . O. Structure-Function Analysis of the Rev-erbA and RVR Ligand-Binding Domains Reveals a Large Hydrophobic Surface That Mediates Corepressor Binding and a Ligand Cavity Occupied by Side Chains. *Molecular Endocrinology* **14**, 700–717 (2000).
27. Woo, E.-J. *et al.* Structural Insight into the Constitutive Repression Function of the Nuclear Receptor Rev-erbβ. *J Mol Biol* **373**, 735–744 (2007).
28. Phelan, C. A. *et al.* Structure of Rev-erbα bound to N-CoR reveals a unique mechanism of nuclear receptor–co-repressor interaction. *Nat Struct Mol Biol* **17**, 808–814 (2010).
29. Shin, Y. *et al.* Small molecule tertiary amines as agonists of the nuclear hormone receptor Rev-erbα. *Bioorg Med Chem Lett* **22**, 4413–4417 (2012).
30. Delmotte, A., Tate, E. W., Yaliraki, S. N. & Barahona, M. Protein multi-scale organization through graph partitioning and robustness analysis: application to the myosin–myosin light chain interaction. *Phys Biol* **8**, 055010 (2011).
31. Srivastava, A., Birari, V. & Sinha, S. Small Conformational Changes Underlie Evolution of Resistance to NNRTI in HIV Reverse Transcriptase. *Biophys J* **118**, 2489–2501 (2020).
32. Srivastava, A. & Sinha, S. Thermostability of In Vitro Evolved Bacillus subtilis Lipase A: A Network and Dynamics Perspective. *PLoS One* **9**, e102856 (2014).
33. Blondel, V. D., Guillaume, J.-L., Lambiotte, R. & Lefebvre, E. Fast unfolding of communities in large networks. *Journal of Statistical Mechanics: Theory and Experiment* **2008**, P10008 (2008).
34. Westermaier, Y. *et al.* Binding mode prediction and MD/MMPBSA-based free energy ranking for agonists of REV-ERBα/NCoR. *J Comput Aided Mol Des* **31**, 755–775 (2017).
35. Rahman, M. H. & Hegazy, L. Mechanism of antagonist ligand binding to REV-ERBα. *Sci Rep* **14**, 8401 (2024).
36. Zhang, T. *et al.* REV-ERB *α* Regulates CYP7A1 Through Repression of Liver Receptor Homolog-1. *Drug Metabolism and Disposition* **46**, 248–258 (2018).
37. Trump, R. P. *et al.* Optimized Chemical Probes for REV-ERBα. *J Med Chem* **56**, 4729–4737 (2013).
38. Dierickx, P. *et al.* SR9009 has REV-ERB–independent effects on cell proliferation and metabolism. *Proceedings of the National Academy of Sciences* **116**, 12147–12152 (2019).
39. He, Y. *et al.* Structure–Activity Relationship and Biological Investigation of a REV-ERBα-Selective Agonist SR-29065 (**34**) for Autoimmune Disorders. *J Med Chem* **66**, 14815–14823 (2023).
40. Bateman, A. *et al.* UniProt: the Universal Protein Knowledgebase in 2023. *Nucleic Acids Res* **51**, D523–D531 (2023).
41. Berman, H. M. The Protein Data Bank. *Nucleic Acids Res* **28**, 235–242 (2000).
42. Gaulton, A. *et al.* ChEMBL: a large-scale bioactivity database for drug discovery. *Nucleic Acids Res* **40**, D1100–D1107 (2012).
43. Pettersen, E. F. *et al.* UCSF Chimera?A visualization system for exploratory research and analysis. *J Comput Chem* **25**, 1605–1612 (2004).
44. Abraham, M. J. *et al.* GROMACS: High performance molecular simulations through multi-level parallelism from laptops to supercomputers. *SoftwareX* **1–2**, 19–25 (2015).
45. Lindorff-Larsen, K. *et al.* Improved side-chain torsion potentials for the Amber ff99SB protein force field. *Proteins: Structure, Function, and Bioinformatics* **78**, 1950–1958 (2010).
46. Berendsen, H. J. C., Postma, J. P. M., van Gunsteren, W. F., DiNola, A. & Haak, J. R. Molecular dynamics with coupling to an external bath. *J Chem Phys* **81**, 3684–3690 (1984).
47. Parrinello, M. & Rahman, A. Crystal Structure and Pair Potentials: A Molecular-Dynamics Study. *Phys Rev Lett* **45**, 1196–1199 (1980).
48. Hess, B., Bekker, H., Berendsen, H. J. C. & Fraaije, J. G. E. M. LINCS: A linear constraint solver for molecular simulations. *J Comput Chem* **18**, 1463–1472 (1997).
49. Ewald, P. Evaluation of optical and electrostatic lattice potentials. *Ann. Phys.* **64**, 253–287 (1921).
50. Parrinello, M. & Rahman, A. Polymorphic transitions in single crystals: A new molecular dynamics method. *J Appl Phys* **52**, 7182–7190 (1981).

51. Lu, C. *et al.* OPLS4: Improving Force Field Accuracy on Challenging Regimes of Chemical Space. *J Chem Theory Comput* **17**, 4291–4300 (2021).
52. Vangone, A. & Bonvin, A. M. Contacts-based prediction of binding affinity in protein–protein complexes. *Elife* **4**, (2015).
53. Charlier, F. *et al.* trevismd/statannotations: v0.6. Preprint at https://doi.org/10.5281/zenodo.8396665 (2023).
54. Srivastava, A. & Sinha, S. Uncoupling of an ammonia channel as a mechanism of allosteric inhibition in anthranilate synthase of Serratia marcescens: dynamic and graph theoretical analysis. *Mol Biosyst* **13**, 142–155 (2017).
55. Cock, P. J. A. *et al.* Biopython: freely available Python tools for computational molecular biology and bioinformatics. *Bioinformatics* **25**, 1422–1423 (2009).
56. Hagberg, A., Swart, P. J. & Schult, D. A. *Exploring Network Structure, Dynamics, and Function Using NetworkX*. (2008).

6. Acknowledgements

The authors acknowledge PARAM Ananta Supercomputational Facility hosted at IIT Gandhinagar as a part of National Supercomputing Mission (NSM), India. S.S. acknowledges the support by Council for Scientific and Industrial Research (CSIR), Ministry of Science and Technology, Government of India, for Junior and Senior Research Fellowship (File No: 09/1031(13466)/2022-EMR-I). R.T. and V.A.M. acknowledge the funding support from IIT Gandhinagar. A.S. thanks Department of Biotechnology for Ramalingaswami Re-entry Fellowship and IIT Gandhinagar for internal project grant support.

7. Author contributions

A.S. conceptualized the project. R.T. and S.S. performed molecular dynamics simulations and molecular docking. A.S., V.A.M., and S.S. performed the analysis. A.S., V.A.M., and S.S. wrote the manuscript.

8. Competing Interests

The authors declare no conflict of interest.

Figures and tables

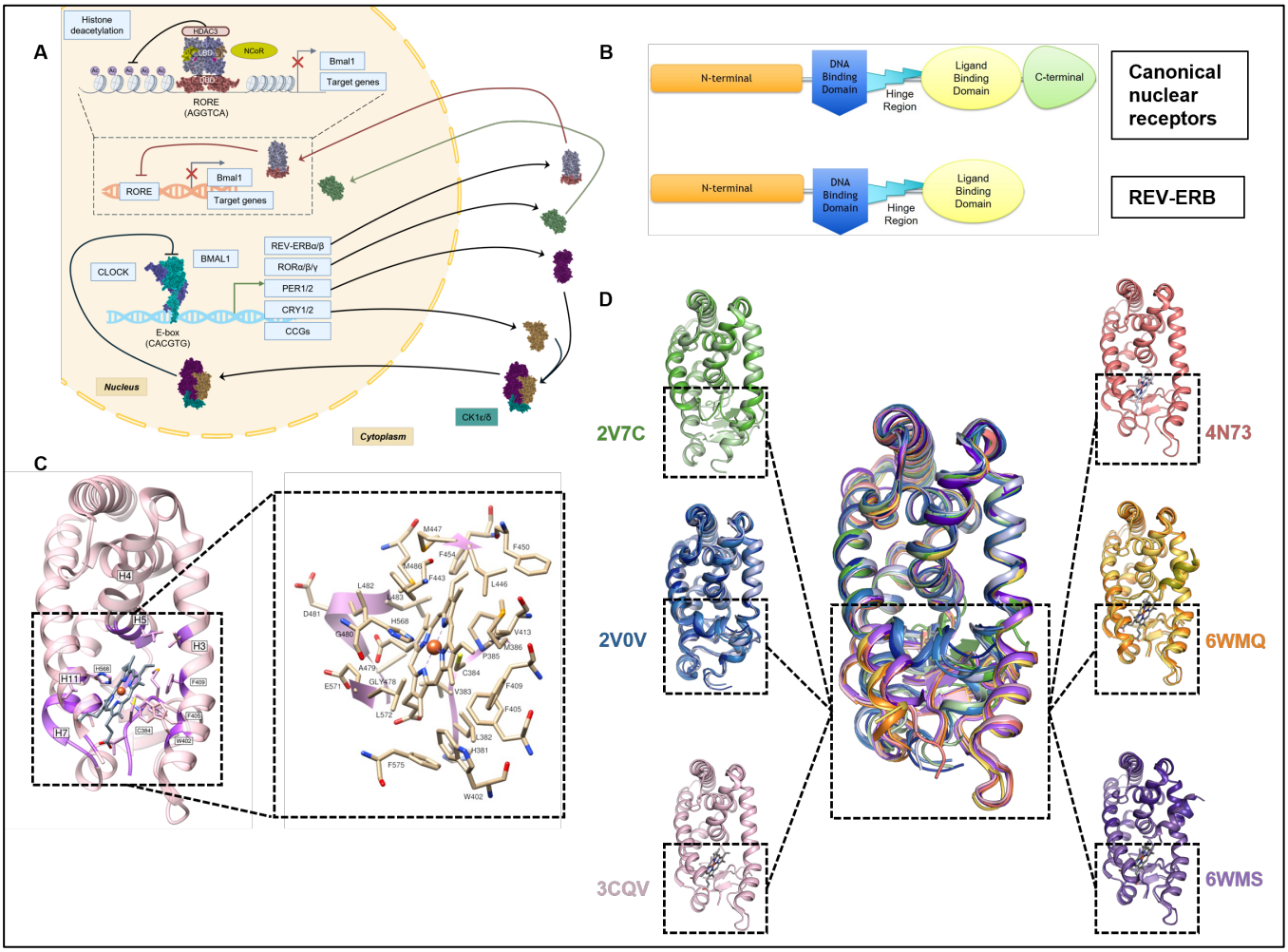

Figure 1: Role of REV-ERBβ as a ligand-dependent transcriptional regulator. (A) Schematic illustration of mammalian circadian transcription-translation feedback loop (TTFL) formed by core-clock proteins: Circadian Locomotor Output Cycles Kaput (CLOCK), BMAL-1, Cryptochrome (CRY1/2), Period (PER1/2), RORE$\alpha/\beta/\gamma$, and REV-ERBα/β. Protein structures for representation in the schematic downloaded from PDB; CLOCK-BMAL1 heterodimer (cyan and blue, PDB ID: 4F3L), CRY1 (golden, PDB ID: 4K0R), PER1 (dark magenta, PDB ID: 4DJ2), RORγ (light green, PDB ID: 3KYT), casein kinase (CK) 1δ (dark green, PDB ID: 4JJR), REV-ERBα DNA binding domain (red, PDB ID: 1GA5), and REV-ERBβ ligand-binding domain (light blue, PDB ID: 6WMQ (heme and NCoR ID1 peptide removed)). Regulatory function of REV-ERBα/β is highlighted in the black box with the detailed view of REV-ERBβ functional dimer comprising heme, NCoR, HDAC3, and RORE response element (schematic protein assembly constructed by combining REV-ERBα DNA binding domain (red, PDB ID: 1GA5), and REV-ERBβ ligand-binding domain structures (light blue, PDB ID: 6WMQ)). Protein structures rendered in PyMOL. **(B)** Comparison of LBD architecture of canonical nuclear receptors and REV-ERB. **(C)** Crystal structure of heme-bound REV-ERBβ

LBD (PDB ID: 3CQV) with key binding site residues and helices are highlighted (heme iron-center denoted by orange sphere, coordinated with C384 and H568 located in the N-terminal loop and Helix-11, respectively). **(D)** Conformational diversity in REV-ERBβ LBD highlighted by crystal structures in Apo (PDB ID: 2V7C (green) and 2V0V (blue)), heme (PDB ID: 3CQV (pink)), cobalt porphyrin (PDB ID: 4N73 (red)) and heme+ID peptide (PDB ID: 6WMQ (orange) and 6WMS (purple)) bound states. Conformational differences in the binding pocket region are highlighted with black boxes. Figure **(A)** created with BioRender.com. Figures **(C)** and **(D)** were rendered in Chimera and PyMOL, respectively.

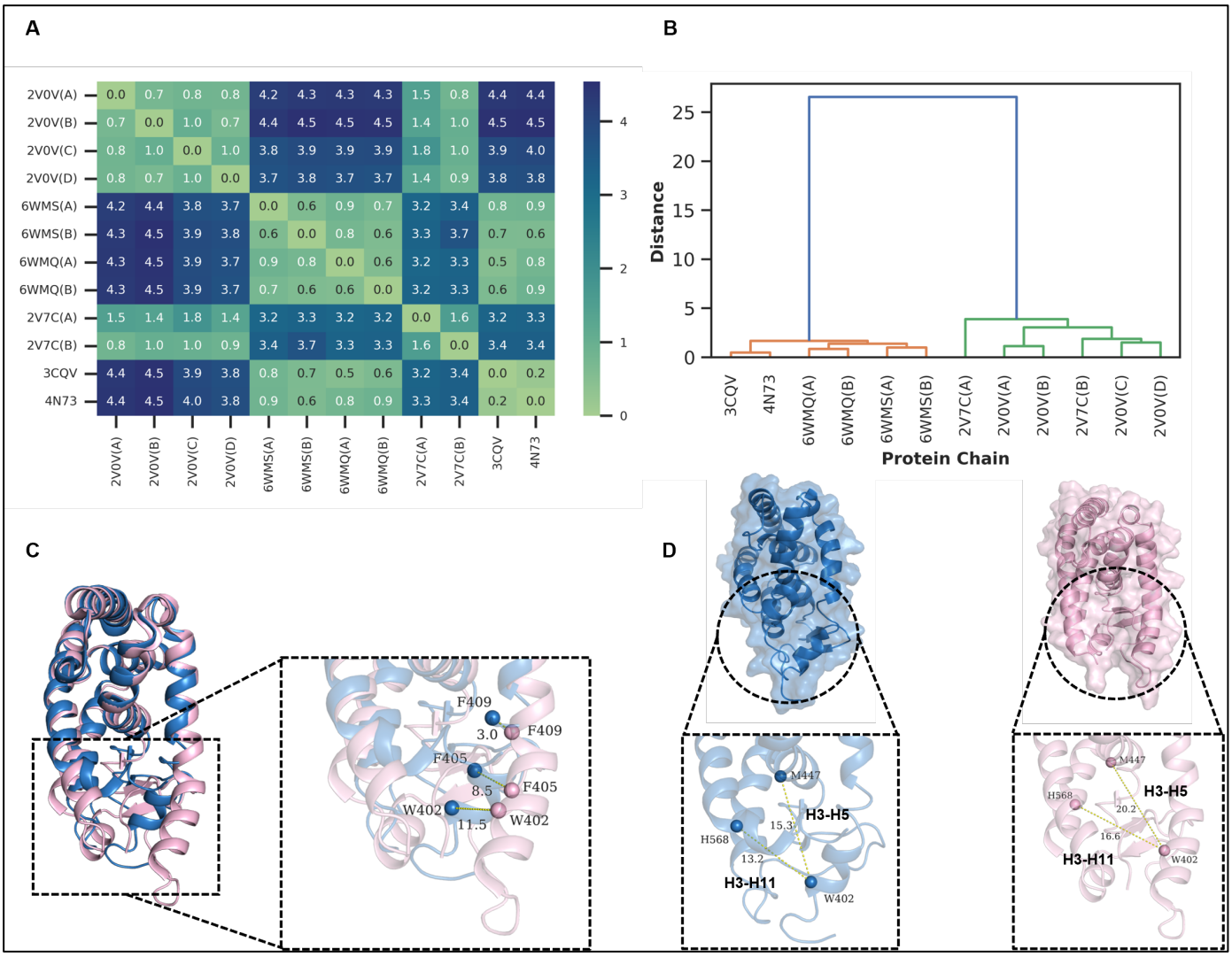

Figure 2: Characterization of REV-ERBβ LBD conformation in different states. (A) Heatmap depicting pairwise Cα-atom RMSD values between individual chains of REV-ERBβ LBD resolved in crystal structures **(B)** Hierarchical clustering of REV-ERBβ LBD chains based on pairwise RMSD matrix. Orange cluster represents heme and heme+ID peptide bound REV-ERBβ LBD chains, while chains in Apo-form are denoted by the green cluster. **(C)** Positional differences of binding site residues (W402, F405, F409) in Helix-3 in Apo (PDB ID: 2V0V-A, blue) and heme-bound (PDB ID: 3CQV, pink) states. **(D)** Surface representation of REV-ERBβ LBD in Apo and heme-bound states with detailed view of distances between H3-H5 and H3-H11 in Apo and heme-bound states highlighting conformational differences. Distances were measured in Å. Heme molecule from heme-bound structure removed for clarity. Figures rendered in PyMOL.

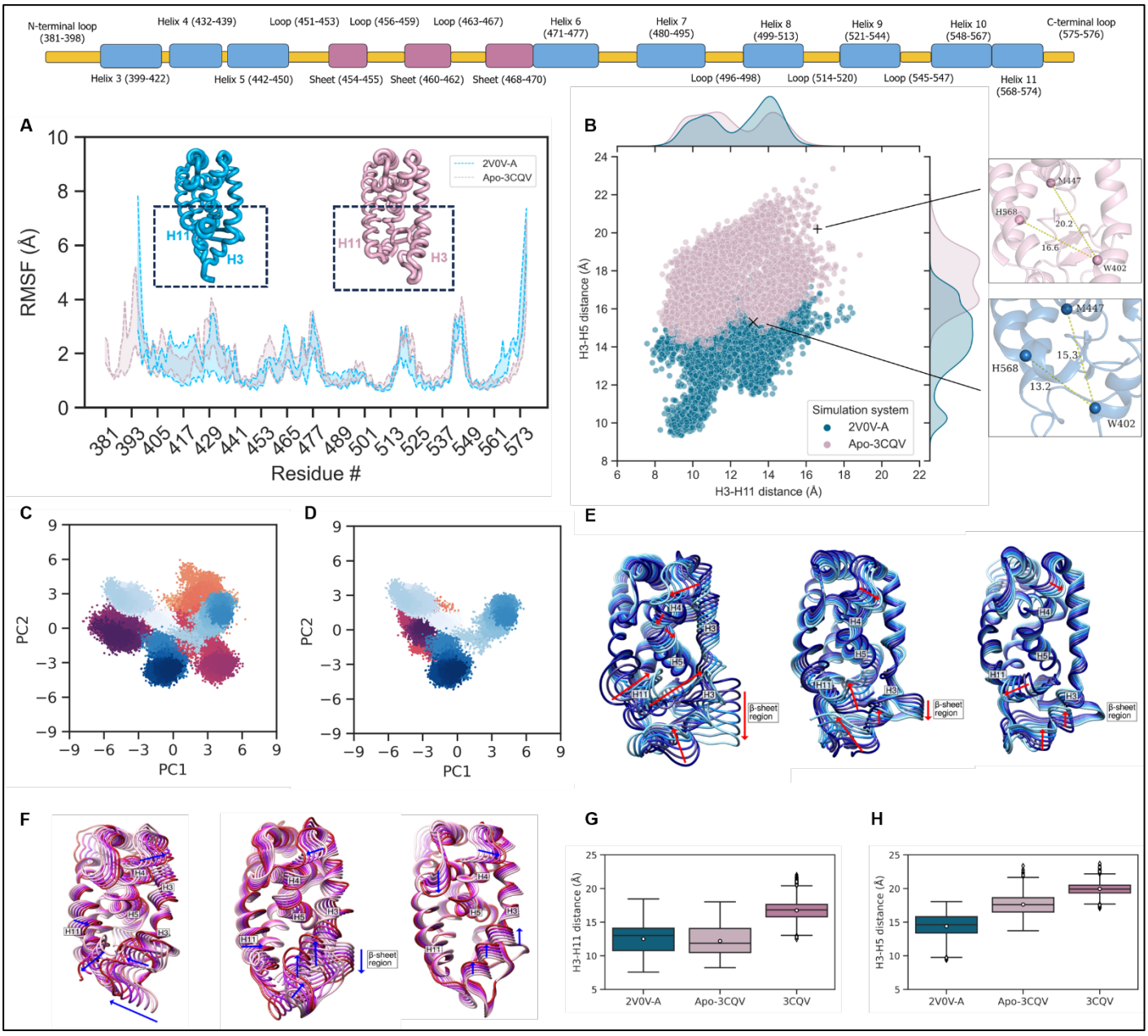

Figure 3: Dynamics of REV-ERBβ LBD in Apo and heme bound states. (A) RMSF plot for REV-ERBβ LBD Cα atoms highlighting flexibility of the binding pocket regions in absence of heme. Region of helices with high fluctuations in 2V0V-A (blue) and Apo-3CQV (pink) MD simulation trajectories are highlighted in black boxes. **(B)** Distances between Cα atoms of W402-M447 (H3-H5) and W402-H568 (H3-H11) in 2V0V-A and Apo-3CQV simulation trajectories. Distances in 2V0V-A and 3CQV crystal structure are denoted by (×) and (+), respectively. **(C)** Projections of 2V0V-A (blue) and Apo-3CQV (pink) MD simulation trajectories on respective first two PCs. **(D)** Projections of 2V0V-A (blue) and Apo-3CQV (pink) MD simulation trajectories on the first two 2V0V-A PCs highlighting overlaps in sampled conformational space. The color gradient in **(C)** and **(D)** represents the timeline of trajectories (2V0V-A timeline depicted by transition from light to dark blue and Apo-3CQV timeline depicted by transition from orange to purple

color). Dominant motions represented by the first three PCs for **(E)** 2V0V-A and **(F)** Apo-3CQV MD simulation trajectories (Left to right: PC1, PC2, PC3). Comparison of **(G)** H3-H11 and **(H)** H3-H5 distances from 2V0V-A (blue), Apo-3CQV (light pink), and 3CQV (dark pink) MD simulation trajectories. The value ranges are represented by whiskers, white dot represent the mean and line within the quartile box denote the median. Figures **(E)** and **(F)** rendered in UCSF Chimera.

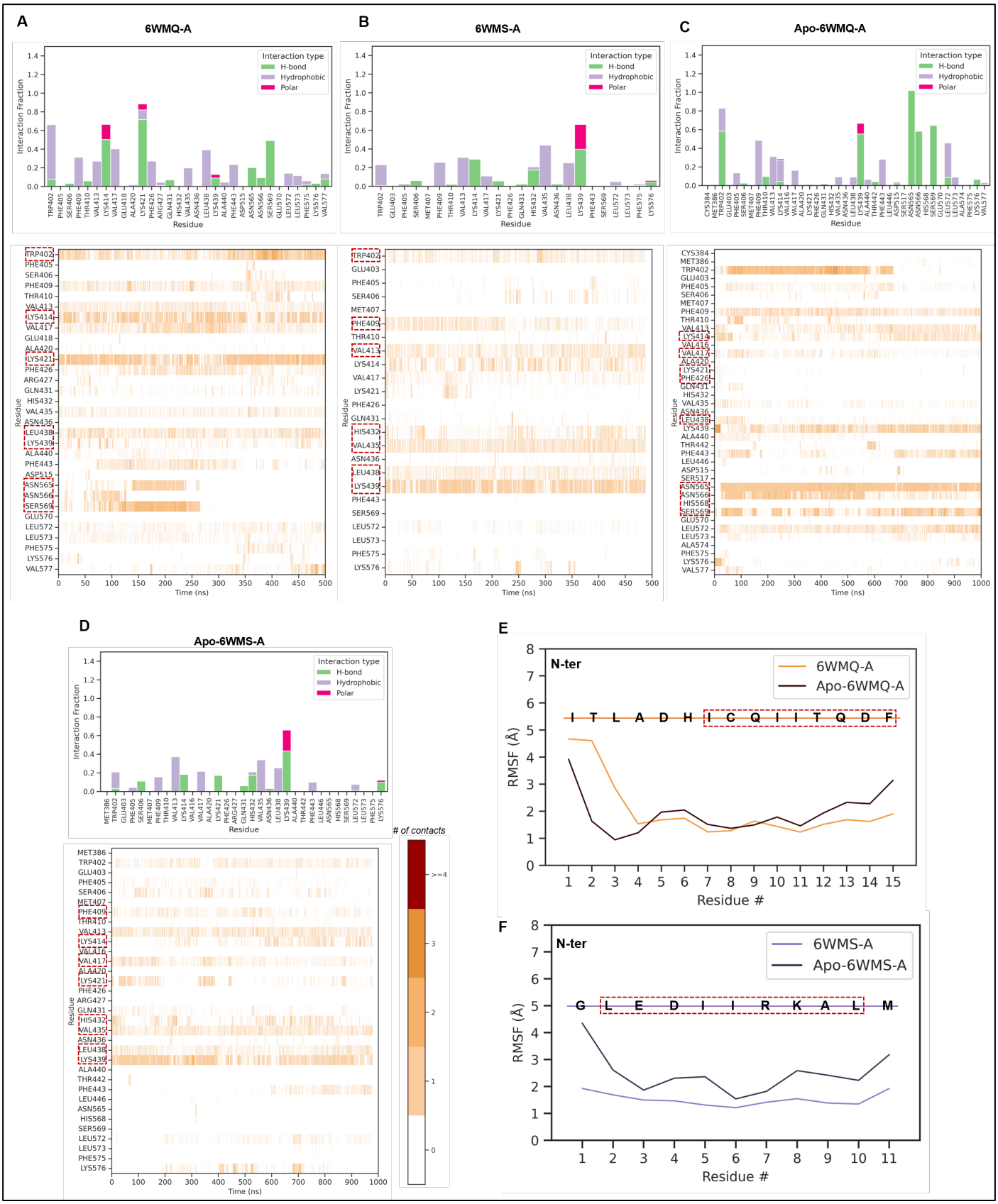

Figure 4: Dynamics of ID1/2 peptide interactions in presence and absence of heme. Interactions of **(A)** ID1 and **(B)** ID2 peptide with REV-ERBβ LBD residues in heme bound MD simulation trajectories (6WMQ-A and 6WMS-A, respectively). Interactions of **(C)** ID1 and **(D)** ID2 peptide with REV-ERBβ LBD residues when heme is removed (Apo-6WMQ-A and Apo-6WMS-A, respectively). The bar graph represents

the type of interactions and heatmap depicts the contact trend of ID1/2 peptide interactions with REV-ERBβ LBD residues across the MD simulation trajectories. REV-ERBβ LBD residues forming AF2 surface for ID peptide binding are highlighted with red boxes. RMSF plot of **(E)** ID1 and **(F)** ID2 peptide Cα atoms in presence (6WMQ-A and 6WMS-A) and absence (Apo-6WMQ-A and Apo-6WMS-A) of heme. The ID peptide residues are shown in the RMSF plots with CoRNR motif highlighted in red boxes.

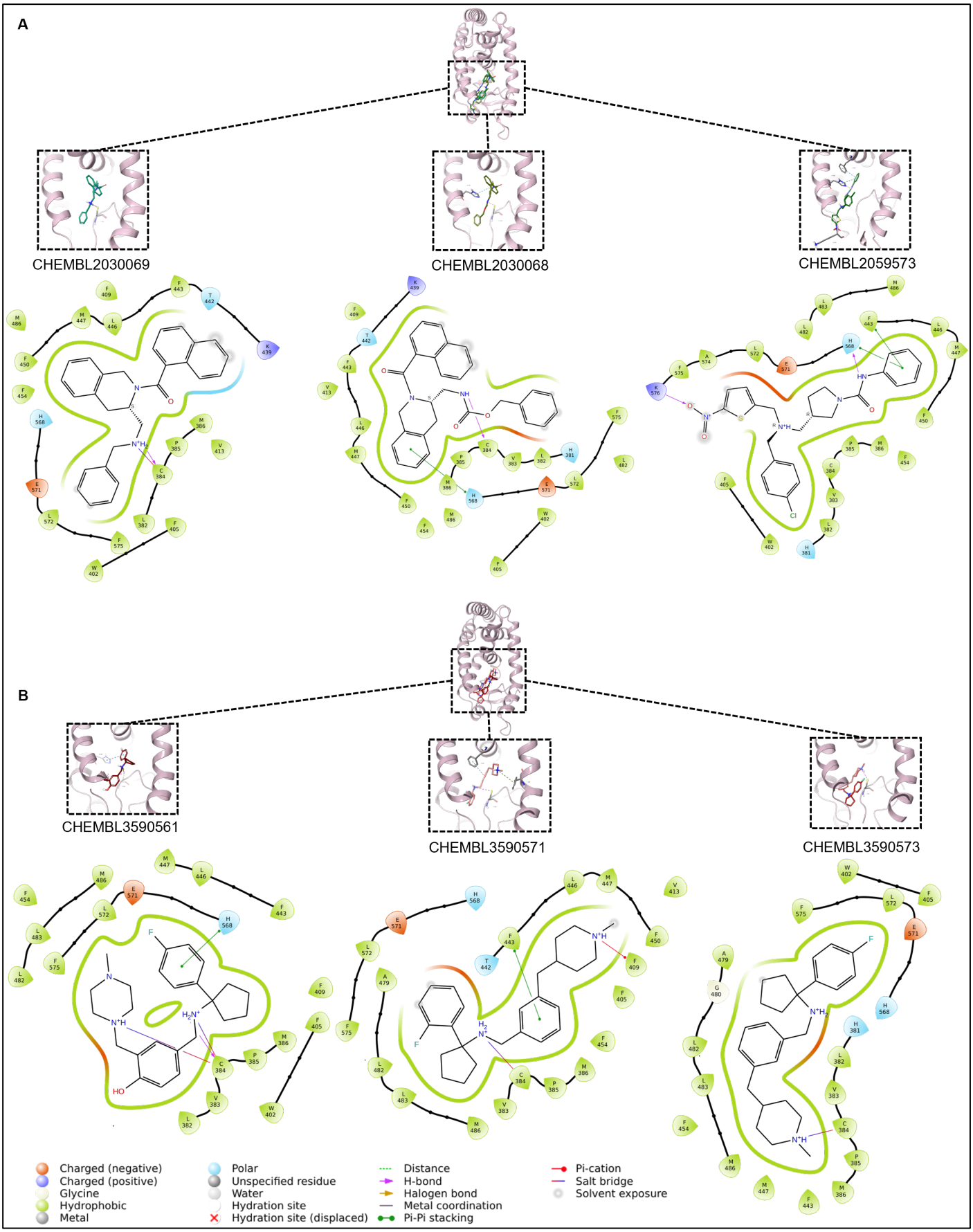

Figure 5: Binding mode of top-three agonists and antagonists with Apo-3CQV from molecular docking screens. Overlay of 3D binding pose of **(A)** top three agonists: CHEMBL2030069, CHEMBL2059573, CHEMBL2030068 and **(B)** top three antagonists: CHEMBL3590561,

CHEMBL3590571, CHEMBL3590573. Detailed 3D binding poses and interactions with REV-ERBβ LBD for each small molecule are highlighted in black boxes. 2D ligand interaction diagram highlights the type of interaction with binding site residues (legend key refers to type of residue and interactions). Docking scores for each small molecule are given in Table 1. Figures rendered in Schrödinger (Schrödinger Release 2022-3).

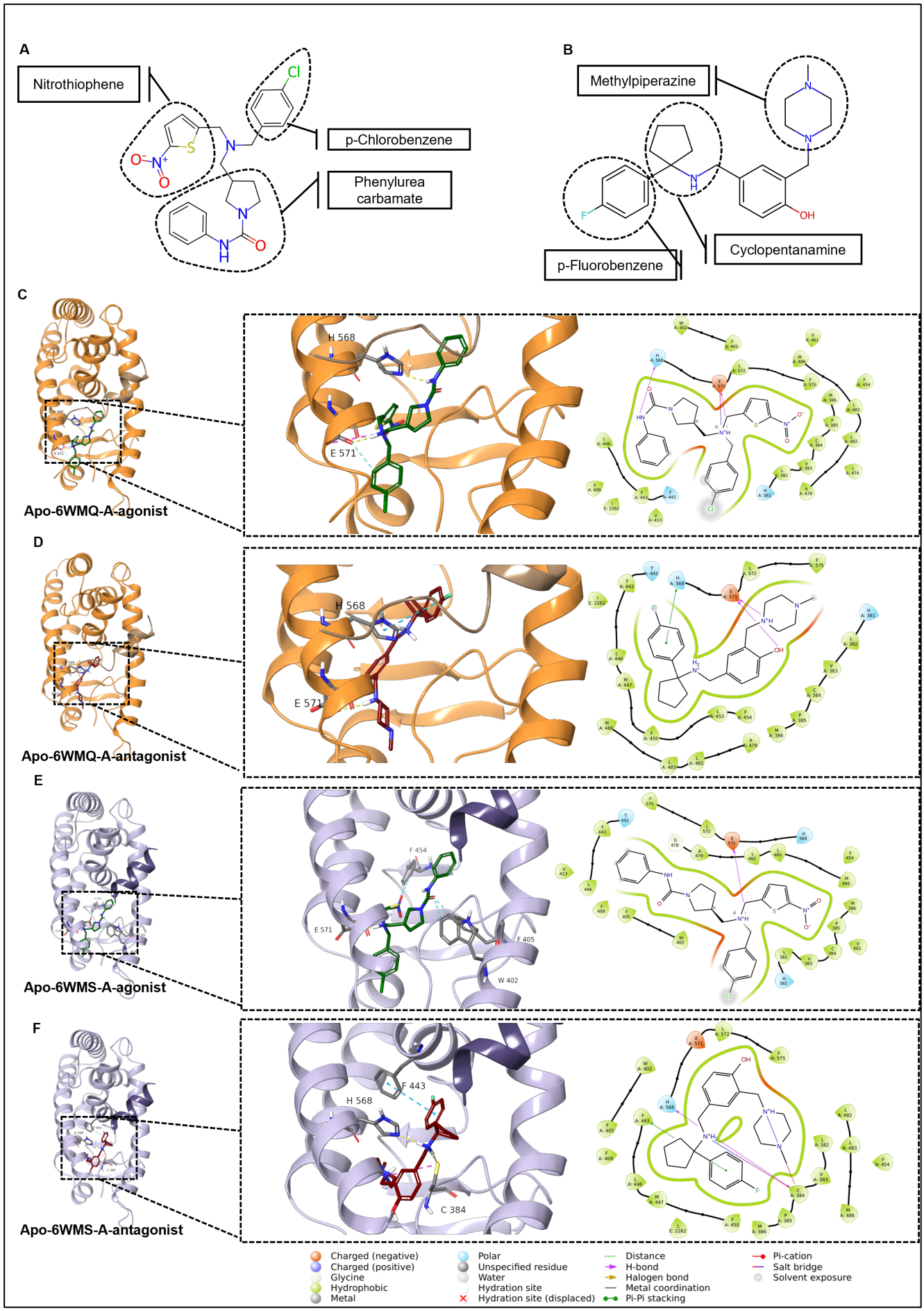

Figure 6: Binding modes of agonist and antagonist in ID peptide bound structure. 2D chemical scaffolds of **(A)** agonist (CHEMBL2059573) and **(B)** antagonist (CHEMBL3590561). Structural features for

each small molecule are highlighted. Docked pose of **(C)** agonist (green) and **(D)** antagonist (red) with ID1 peptide bound Apo-6WMQ-A structure (orange). Docked pose of **(E)** agonist (green) and **(F)** antagonist (red) with ID2 peptide bound Apo-6WMS-A structure (purple). 3D binding poses and 2D ligand interactions with REV-ERBβ LBD and ID peptide for each small molecule are highlighted in black boxes (legend key refers to type of residue and interactions). Figures **(C)-(F)** (rendered in Schrödinger (Schrödinger Release 2022-3).

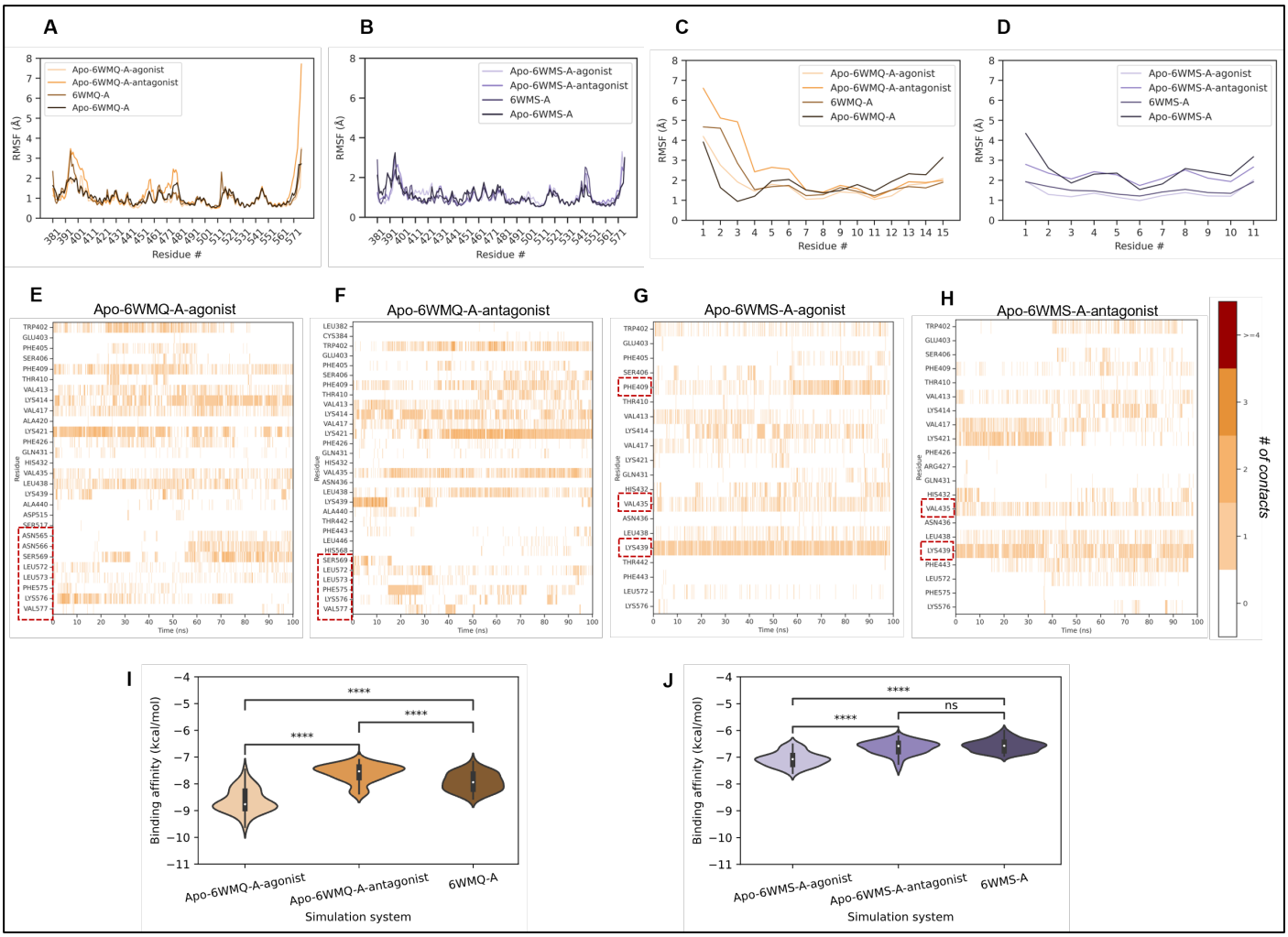

Figure 7: Comparative analysis of Apo-6WMQ-A and Apo-6WMS-A MD simulation trajectories in presence of agonist and antagonist. Combined RMSF plot for REV-ERBβ LBD Cα atoms from **(A)** ID1 and **(B)** ID2 bound simulation trajectories in presence of agonist, antagonist, heme, and absence of any ligand. RMSF plot of **(C)** ID1 and **(D)** ID2 peptide Cα atoms in presence of agonist, antagonist, heme, and in absence of any ligand. ID1 peptide interactions with REV-ERBβ LBD residues in presence of **(E)** agonist (Apo-6WMQ-A-agonist) and **(F)** antagonist (Apo-6WMQ-A-antagonist). ID2 peptide interactions with REV-ERBβ LBD residues in presence of **(G)** agonist (Apo-6WMS-A-agonist) and **(H)** antagonist (Apo-6WMQ-A-antagonist). The heatmap depicts contact trend of ID1/2 peptide interactions with REV-ERBβ LBD residues across the MD simulation trajectories. Key differences in ID peptide interactions are highlighted with red boxes. Comparison of binding affinity of **(I)** ID1 and **(J)** ID2 peptide in different simulation systems. The Mann-Whitney-Wilcoxon two-sided statistical test was performed for comparison. **** indicates p-val less than or equal to 0.0001, ns indicates not significant.

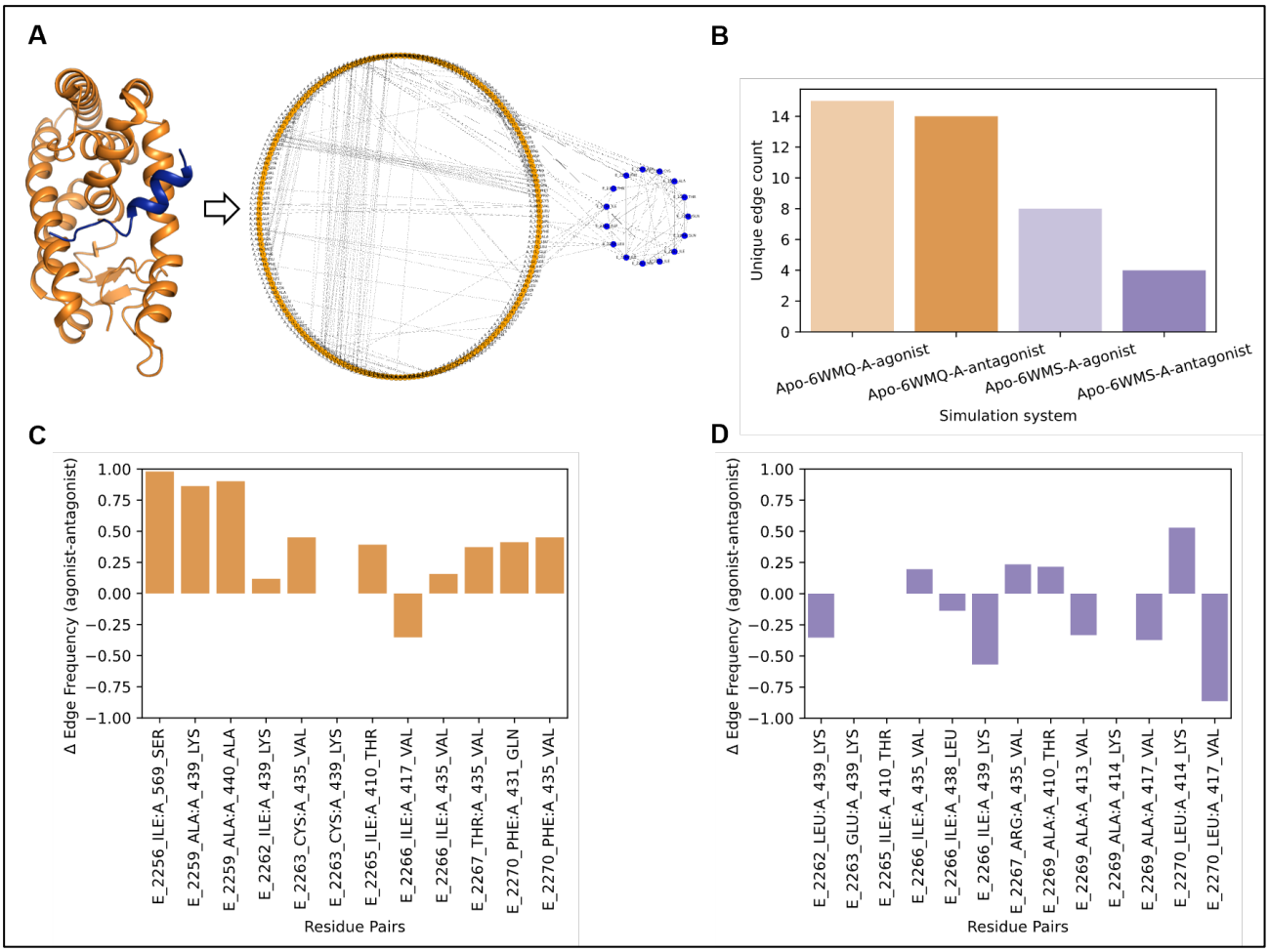

Figure 8: Comparative analysis of Apo-6WMQ-A and Apo-6WMS-A agonist/antagonist protein contact network. (A) Schematic illustration of 3D protein structure decomposed to a 2D dimensional network. **(B)** Comparison of number of unique edges between LBD (chain A) and ID1/2 (chain E) in the presence of agonist/antagonist **(C)** Difference in the edge frequency of the common edges between Apo-6WMQ-A-agonist and Apo-6WMQ-A-antagonist. **(D)** Difference in the edge frequency of the common edges between Apo-6WMS-A-agonist and Apo-6WMS-A-antagonist.

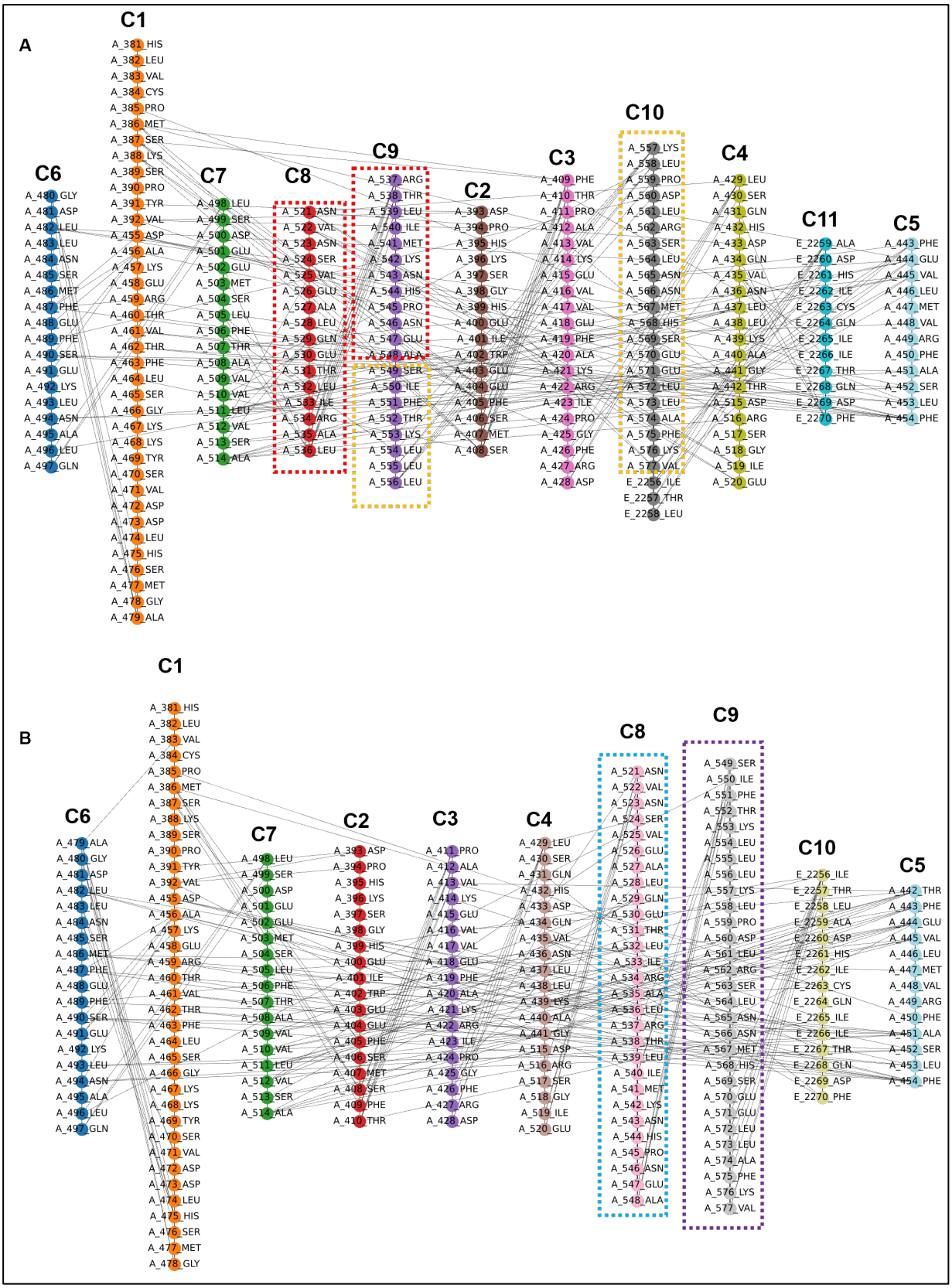

Figure 9: Community membership in Apo-6WMQ-A-agonist/antagonist protein contact network. Community structure of **(A)** Apo-6WMQ-A-agonist (top) and **(B)** Apo-6WMQ-A-antagonist (bottom). Community C10 (grey) in Apo-6WMQ-A-agonist harboring LBD and ID peptide residues in a single community. Residues marked with red, and orange dotted lines in Apo-6WMQ-A-agonist reorganized as a

single community C8 and C9 in Apo-6WMQ-A-antagonist marked with blue and purple dotted lines, respectively.

2 **Table 1: Docking score of small molecules in different complexes**

ChEMBL ID	Molecule type	Apo-3CQV	Apo-6WMQ-A	Apo-6WMS-A
2030069	Agonist	–10.5	–2.8	–10.2
2059573	Agonist	–9.7	–8.6	–8.9
2030068	Agonist	–9.1	–2.2	–8.8
3590561	Antagonist	–9.7	–8.3	–10.0
3590571	Antagonist	–9.4	–7.6	–9.0
3590573	Antagonist	–8.3	–7.9	–9.7

3